Reviewed Preprint
v1 • September 25, 2025
Not revised

Reviewed Preprint
v2 • July 28, 2026
Revised by authors

Product-stabilized filamentation by human glutamine synthetase allosterically tunes metabolic activity

Eric Greene[1,*], Richard Muniz[2], Hiroki Yamamura[1], Samuel E Hoff[3], Priyanka Bajaj[1], Markus Tecson CB Tecson[4], Cyrina Geluz[4], D John Lee[1], Erin M Thompson[1], Angelika Arada[1], Gyun Min Lee[5], Massimiliano Bonomi[3], Justin M Kollman[2], James S Fraser[1]

[1]Department of Bioengineering and Therapeutic Sciences, University of California, San Francisco, San Francisco, United States • [2]Department of Biochemistry. University of Washington, Seattle, United States • [3]Institut Pasteur, Université Paris Cité, CNRS UMR 3528, Computational Structural Biology Unit, Paris, France • [4]Department of Chemistry and Biochemistry, San Francisco State University, San Francisco, United States • [5]Department of Biological Sciences, KAIST, Daejeon Republic of Korea

For correspondence: jfraser@fraserlab.com

* Present address: Department Chemistry and Biochemistry, San Francisco State University, San Francisco, CA

Competing interests: HY is an employee of JSR. J.S.F. is a consultant to, a shareholder of, and receives sponsored research support from Relay Therapeutics.

Funding: See page 23

Reviewing editor: Luke Wiseman, Scripps Research Institute, United States

eLife Assessment

This manuscript employs cryo-EM, mutational analysis, and biochemical assays to explore the molecular basis by which glutamine promotes filamentation and regulates the activity of human glutamine synthetase (hGS) by stabilizing interactions between hGS decamers. The combined structural and biochemical data supporting the proposed mechanism are **solid**, although the evidence for a higher-order filamentous architecture and the precise assignment of the interface density would benefit from additional support. This work will be of particular interest and **useful** to groups interested in understanding the molecular basis of nutrient sensing, cellular metabolism, and structural regulation of enzyme activity.

https://doi.org/10.7554/eLife.108336.2.sa4

Abstract

To maintain metabolic homeostasis, enzymes must adapt to fluctuating nutrient levels through mechanisms beyond gene expression. Here, we demonstrate that human glutamine synthetase (GS) can reversibly polymerize into filaments aided by a composite binding site formed at the filament interface by the product, glutamine. Time-resolved cryo-electron microscopy (cryo-EM) confirms that glutamine binding stabilizes these filaments, which in turn exhibit reduced catalytic specificity for ammonia at physiological concentrations. This inhibition appears induced by a conformational change that remodulates the active site loop ensemble gating substrate entry. Metadynamics ensemble refinement revealed >10 Å conformational range for the active site loop and that the loop is stabilized by transient contacts. This disorder is significant, as we show that the transient contacts which stabilize this loop in a closed conformation are essential for catalysis both *in vitro* and in cells. We propose that GS filament formation constitutes a negative-feedback mechanism, directly linking product concentration to the structural and functional remodeling of the enzyme.

Introduction

To support the metabolic needs of a cell, enzymes must be regulated to adapt to changing nutrient conditions (Atkinson 1965). Because these changes often occur faster than the rates of transcription/translation or degradation, this regulation is conferred allosterically by downstream metabolites or posttranslational modifications, or orthosterically via substrate availability and/or

product inhibition (Mathy and Kortemme 2023). In metabolism, one common allosteric mechanism is feedback inhibition whereby downstream metabolites alter the enzymatic activity of upstream processes, typically at rate-limiting or committed metabolic nodes (Gerhart and Pardee 1962). In classical models of allostery, this regulation is conferred through the binding of an effector molecule at a site other than the protein's active site, known as the allosteric site (Cui and Karplus 2008). Allosteric ligand binding subsequently induces or stabilizes a conformational change in the protein that can manifest at the tertiary, quaternary, and/or quinary (e.g. filamentous or other supramolecular states) level leading to the activity change observed (Hvorecny and Kollman 2023).

While many well-studied metabolic enzymes have evolved dedicated small molecule or protein allosteric binding sites as a primary means of regulation, an increasing number of soluble metabolic enzymes have been observed to adopt supramolecular, filamentous quinary structures as a mechanism for allosteric regulation (Noree et al. 2019; Park and Horton 2019). Filament formation can confer multiple distinctive mechanisms of enzyme regulation including repression and activation, providing an alternative to synthesis/degradation to rapidly alter the balance of enzyme activity within the cell (Lynch et al. 2020; Hvorecny and Kollman 2023). Indeed, more classic small molecule binding sites can regulate enzyme filamentation and the combination of these two modes represents a rich expansion of classical allostery, integrating structural and functional changes at the level of protein assembly.

Here, we examine how glutamine metabolism is controlled by different potential allosteric mechanisms. Glutamine levels must be critically regulated, as it uniquely serves as both an anaplerotic donor (carbon source) and a nitrogen donor in key metabolic processes (Tecson et al. 2025; Fung et al. 2025). In addition, it is, obviously, a building block in protein biosynthesis. Glutamine synthetase (GS) is an ancient enzyme that catalyzes the ATP-dependent condensation of glutamate and ammonia to glutamine (Eisenberg et al. 2000; de Carvalho Fernandes et al. 2022; Tecson et al. 2025). Glutamine is the most abundant amino acid in blood, where a majority originates from *de novo* synthesis by GS (Tecson et al. 2025; Fung et al. 2025; Castegna and Menga 2018). Moreover, ammonia generated through catabolic processes is detoxified through GS-catalyzed glutamine formation. The ammonia detoxification is critically important in the brain, where loss of function GS variants cause severe developmental defects (Spodenkiewicz et al. 2016). Regulation of human GS has so far been largely described at the transcriptional or protein degradation levels (Eisenberg et al. 2000; Rigual et al. 2025; Castegna and Menga 2018) where GS expression is restricted to certain cell types and tissues and expressed GS can be degraded by the ubiquitin proteasome system in a glutamine dependent manner (Zhao et al. 2025; Van Nguyen et al. 2016, 2017; Van Nguyen 2021). However, regulation via these processes would require hours to achieve appreciable changes in intracellular GS concentrations. By contrast, multiple allosteric and feedback mechanisms have been described for bacterial GS homologs, including by filamentation in both *E. coli* (Eisenberg et al. 2000; Huang et al. 2022) and *S. cerevisiae* (Petrovska et al. 2014; He et al. 2009). These observations led us to ask how human GS activity could be regulated on the timescales required to adapt to dynamic changes in nutrient availability.

Here, we used a combination of cryo-electron microscopy (cryoEM), enzymology, and cell proliferation assays, to discover a regulatory mechanism that incorporates both feedback inhibition and filamentation. We find that human GS forms filamentous assemblies that are stabilized by its own reaction product, glutamine. Human GS filaments display lower catalytic efficiency for ammonia, which we attribute to changes in protein flexibility surrounding the active site. We probe the importance of this change in protein dynamics with mutagenesis using enzyme activity *in vitro* and in HEK293 cells. Our findings support a model where product-stabilized GS filaments serve as an allosteric feedback mechanism, regulating activity through modulation of the enzyme's conformational landscape.

Results

Identification of heterogeneous oligomeric assemblies of human GS

To define regulatory mechanisms of GS, we first used cryoEM to examine the conformational landscape of GS. Our initial attempts at *in vitro* characterization of GS using N-terminally His_6-tagged constructs were met with low molecular weight complex compositions by size-exclusion chromatography (SEC) and we observed rare, decameric 2D averages by negative-stain electron microscopy (Figure 1A, B). However, most particles and 2D classes were distorted and this preparation did not result in a large population of the canonical decameric form observed in the X-ray structure of the identical GS construct (Krajewski et al. 2008). However, scarless preparations of GS, either through N-terminal His_6-SUMO-tag and Ulp1 cleavage during purification or C-terminal Intein-CBD-His_6 tag and DTT facilitated intein self-cleavage yielded pure enzyme with both decameric and higher molecular weight species observed by SEC (Figure 1A, B). In addition to scarless preparations yielding canonical forms of GS, we found a >5-fold higher $k_{cat}/K_{M,glutamate}$ for scarless GS, and that the His_6-tagged counterpart has a decoupled reaction whose ADP-release was insensitive to ammonia concentration (Figure 1C, Supplementary Figure 1). These data demonstrate a significant structural and functional impact of N-terminal His_6 tags on GS in addition to the presence of supramolecular architectures.

To investigate how differences in oligomeric state might impact the structure and function of GS, we characterized the decamer oligomeric fraction isolated by SEC by cryoEM. We observed GS to be present in decameric form, but also a resolvable population of short filament assemblies of repeating decameric units. These higher order assemblies are consistent with dynamic exchange corresponding to the distribution of SEC peaks with estimated molecular weights of ~0.3 - 1.5 MDa (Figure 1B). We isolated the 2-decameric/di-decameric particles from the decameric particles using 2D classification and non-heterogeneous refinement and reconstructed a high resolution map with $FSC_{0.143}$ of 2.38 Å (Supplementary Figure 2 and Supplementary Figure 3).

The filament was composed of two decamers ("2-decamer") bound to each other in a 'head-to-head' configuration with one decamer rotated ~26° to the next (Figure 1D). The decamer-decamer (filament) interface is five-fold symmetric and made up of residues K52, C53, and E55 contributed by both monomeric subunits across the interface. Interestingly, K52 also participates in a binding interface between GS and bestrophilin2 ion channel (Owji et al. 2022). We observed little to no density at the interface despite the stable relative orientation of both decamers to each other (Figure 1D). These data suggest that the formation of the interface is concentration dependent and driven primarily by electrostatic interactions.

Alternatively, the interface could be largely solvent-mediated or be connected by a ligand(s) that occupy only some of the 5 symmetry related interfaces. In both scenarios, any signal is likely to be averaged out and experiments with symmetry expansion and focused classification did not yield any convincing density.

To test the importance of the interface, we used homo-bifunctional crosslinking to probe the contributions of individual contacts. The 2-decameric map suggests that only one pair of lysine residues (K52:K52) and one pair of cysteine residues (C53:C53) are surface exposed and within <10Å across two monomers. To ensure a stringent selection for only K52 and C53 we used either the 7.7Å spacer-arm bifunctional NHS-ester crosslinker (bis(sulfosuccinimidyl) glutarate or BSG) or the 8.0Å spacer-arm biofunctional maleimide crosslinker (bismaleimidoethane or BMOE). Crosslinking of two monomers by either crosslinker was observed in the wild-type enzyme and more prevalent at higher enzyme concentrations (Figure 1E). However, mutation of either K52 or C53 to alanine ablated the crosslinking reactivity and reduced filament formation as assessed by negative stain EM (Supplementary Figure 5). Together these data support the 2-decameric filament interface assignment whose formation is concentration dependent and driven primarily by electrostatic interactions.

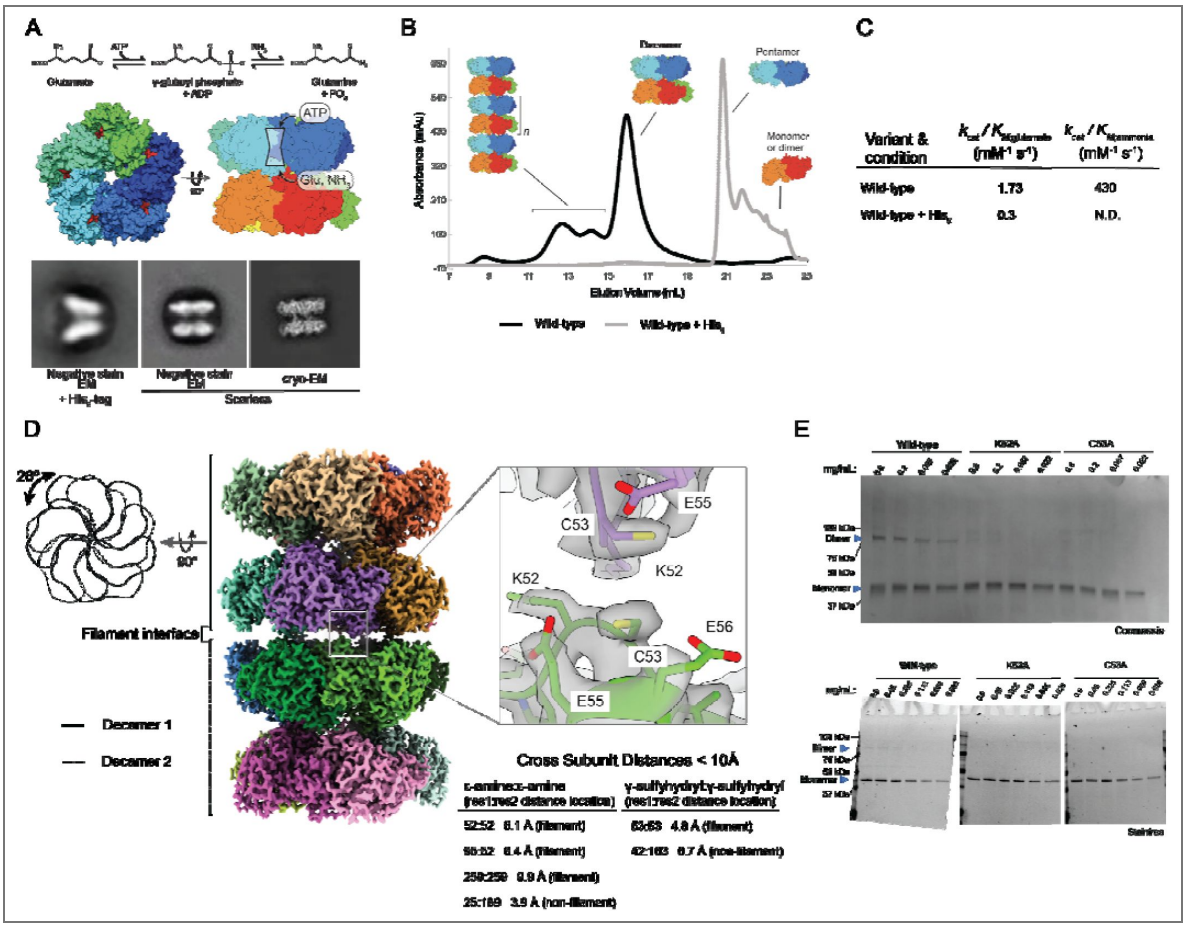

Figure 1. Human Glutamine Synthetase Forms Filaments.

A) At top, reaction mechanism of glutamine synthetase. Middle: surface representation of PDB:2QC8 ADP + Methionine sulfoximine (MSO) bound X-ray crystal structure of human glutamine synthetase. Bottom: N-terminal His_6-tag perturbs structure of human glutamine synthetase (GS) as observed by 2D classification of negative stain and cryoEM data. B) Size-exclusion chromatography reveals His_6-tag dramatically alters the oligomeric state of human GS and scarless GS can form higher order oligomers. C) His_6-tagged GS displays strongly altered steady-state kinetic constants when compared to scarless GS. N.D. = not defined as His_6-tagged GS also display inefficient coupling of ATP hydrolysis with glutamine formation and thus $K_{M,ammonia}$ could not be defined for this enzyme. D) cryoEM reconstruction of apo-GS filament form. Decamers are rotated relative to each other by ~26 degrees. The minimal five-fold filament interface formed consists of K52, C53, and E55 of adjacent monomers from different decamers. No obvious connecting cryoEM density is observed in the apo map. Cross Subunit Distances that are less than 10 LJ between cysteine residues or lysine residues are listed as potential crosslinking sites for bifunctional crosslinkers Bis-sulfosuccinimidyl glutarate (BSG) or bis-maleimoethane (BMOE) E) Bifunctional crosslinking with BSG (top) or BMOE (bottom) to covalently attached adjacent primary amines (K52) or cysteines (C53) respectively followed by SDS-PAGE reveals crosslinked species only in the wild-type GS protein sample, but not K52A or C53A indicating presence and disruption of filament formation respectively.

Glutamine stabilizes larger GS filaments

The interface defined by the 2-decameric assembly and the presence of higher molecular weight species in the SEC trace suggested that larger filaments of GS can readily form. Next, we wanted to understand what functional consequence may be conferred by filamentation in human GS. We asked if GS filament formation could be retained under turnover conditions and impact the catalytic function of GS. CryoEM is an ideal tool to investigate structural changes to macromolecules under turnover conditions because substrates can be added to the enzyme immediately before vitrification freeze-quenching to preserve the sample in a near-native context (Figure 2A, Supplementary Figure 6). Turnover conditions were induced by adding saturating concentrations of substrates immediately prior to vitrification, with reaction times totalling between 49 and 59s initiated by manual mixing prior to blotting.

Our initial grid screening of GS under turnover conditions identified filaments at lower GS concentrations (0.1 mg/mL) than we observed for apo GS. Initial reconstruction of these screening data revealed two new structural features in the GS filament: defined EM density between both decamers and missing density for the active site loop region (Figure 2A).

Given that the only sample preparation differences between the apo-GS datasets and the turnover conditions was the addition of substrates that are converted to products prior to vitrification, we hypothesized that one or multiple substrates (ATP, glutamate, and ammonium) or products (glutamine, PO_4, and ADP) may be responsible for this additional density. However, at this initial low resolution we could not assign a compound at this interface nor understand if an interface-bound compound had any conformational impact on active site geometry.

To discriminate whether the additional filament density corresponded to product or substrate, we performed a time-resolved (tr-)cryoEM experiment. We collected five turnover cryoEM datasets that differed only in the vitrification-quench time of the steady-state reaction with reaction times between 57s and 517s corresponding to high substrate and high product respectively (see methods for details) at a fixed concentration of enzyme (0.3 mg/mL). To understand if there was a trend in the particle populations between the decamer/filament compositions as a function of reaction time, we compared the number of particles in decameric versus filamentous states by 2D classification (Supplementary Figure 7). The same template picking parameters were applied for each tr-cryoEM dataset and 2D classification was performed thrice; once with each time-point dataset processed independently and twice where all particles were combined and the dataset identity only revealed after 2D classification particle classes were picked and 2D classes were picked with and without top views (Supplementary Figure 9 and Supplementary Figure 10). We then normalized decamer and filament particle picks to the total number of picked particles (excluding 2D classes that could not be assigned either a decamer or filament) and plotted these as a function of reaction time (Figure 2B). The positive linear correlation between fraction of particles in a filament-like assembly and reaction time suggests that a product of the forward reaction of GS acts to stabilize the filament assembly. Subsequent screening with high concentrations of glutamine revealed large >4 decameric unit filament assemblies (Figure 2C), suggesting that product formation has a positive effect on filament assembly.

To define how products stabilized the GS filament assembly, we next determined a high resolution structure of the filaments imaged under turnover conditions. We performed an additional cryoEM experiment with increased GS concentration (1.5 mg/mL), to bias our particle populations towards filamentous assemblies, and vitrified at 57s, a reaction time that should yield a high concentration of product due to the higher enzyme concentration than previous experiments. The resulting 3D reconstruction of the 2-decameric species had an $FSC_{0.143}$ of 2.2Å (Supplementary Figure 11A and Supplementary Figure 8).

Inspection of the 'filament assembly' interface between the two decamers revealed a discrete density that was absent from the apo-filament reconstruction (Figure 2D). The density is too small for a nucleotide (ATP or ADP) and too large for inorganic phosphate (Supplementary Figure 11B). Given the association with product formation, we modeled glutamine into this density in a conformation consistent with forming hydrogen bonds that link the filament interface residues

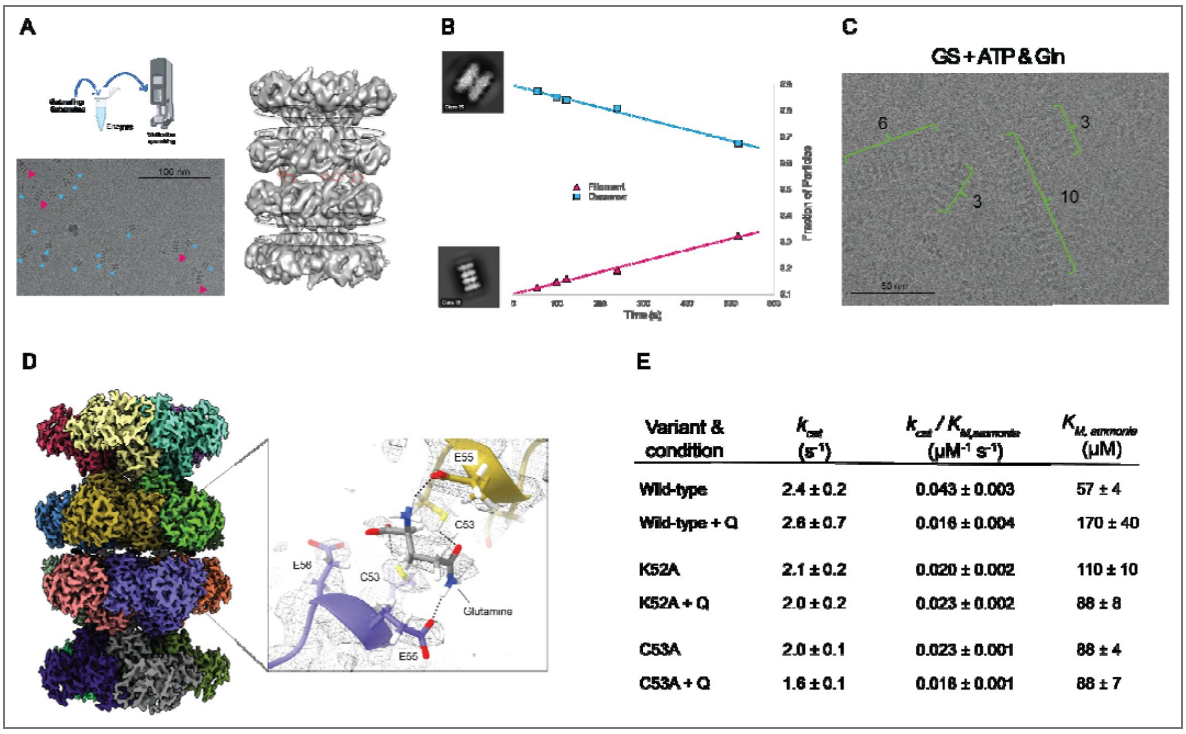

E

Variant & condition	k_{cat} (s^{-1})	k_{cat} / $K_{M,ammonia}$ (μM^{-1} s^{-1})	$K_{M,\ ammonia}$ (μM)
Wild-type	2.4 ± 0.2	0.043 ± 0.003	57 ± 4
Wild-type + Q	2.6 ± 0.7	0.016 ± 0.004	170 ± 40
K52A	2.1 ± 0.2	0.020 ± 0.002	110 ± 10
K52A + Q	2.0 ± 0.2	0.023 ± 0.002	88 ± 8
C53A	2.0 ± 0.1	0.023 ± 0.001	88 ± 4
C53A + Q	1.6 ± 0.1	0.018 ± 0.001	88 ± 7

Figure 2. Glutamine binds to GS filaments at the interface.

A) Establishment of steady state conditions prior to vitrification with GS at low concentration (0.15 mg/mL) revealed presence of 2-decameric species (red arrows) in addition to decameric species (blue arrows) during cryoEM grid screening. Initial reconstruction of the turnover 2-decameric map demonstrated clear density connecting decamers (red dotted circle) not previously observed in the apo-filament map and loss of E305-loop density (black dotted circle). B) Time-resolved cryoEM demonstrates linear relationship between glutamine and filament formation assessed by independently processing five datasets and quantifying the fraction of decamer and filament present (see Methods) and plotted against the vitrification quench time of the reaction. C) cryoEM screening data demonstrating robust filament seeding from addition of ATP and glutamine to human GS prior to vitrification. D) Turnover-filament global 3D reconstruction (left) and locally refined filament interface (right) demonstrates similar overall architecture to apo-filament map (left) but with clear density between decamers with glutamine modeled which forms hydrogen bonds with K52, C53, and E55 (right). E) Steady-state ammonia kinetic constants for wild-type, K52A, and C53A with and without 10 mM glutamine added to reaction to stimulate filament formation. Errors were calculated as S.E.M. from global fitting and were propagated through each Michaelis-Menten parameter (Equations 2-4; n = 8 replicates) see Methods.

and the bound product (Supplementary Table 2). The two-fold symmetry at this interface and the averaging inherent in our data processing results in density that likely reflects contributions from glutamine in two orientations. To relieve symmetry averaged artefacts, we symmetry expanded particles and subjected them to focused refinement on a single binding site with a mask covering four subunits total to support particle alignment (Figure 2E). The resulting density was supported by glutamine positioning similar to the symmetry refined global map (Supplementary Table 2) . In addition, we note two potential, and not mutually exclusive, reasons we were able to observe filaments in the apo enzyme. First, we used high concentrations of GS, which likely shifts the equilibrium towards the filament form even in the absence of glutamine. Second, there may be a small, unresolved, amount of glutamine that persists during purification that occupies only a minor fraction of interfaces per di-decamer. As discussed above, such contributions would be averaged out during map refinement in the scheme we have used here. Taken together, these data support a model wherein glutamine synthetase filamentation generates a composite binding site for glutamine at the filament interface, which is located over 10Å from the active site.

Glutamine stabilized filaments have lower catalytic efficiency for ammonia

We next examined the functional consequences of GS filamentation on enzymatic activity. To assess steady-state kinetic differences between decameric and filamentous compositions of GS, we assayed different isotropic peak fractions resolved by SEC immediately after separation. We found k_{cat} and k_{cat}/K_M for all substrates were completely in agreement between the decamer and 2-decamer fractions at 0.01 mg/mL for wild-type, K52A, and C53A (Supplementary Figure 13). However, this enzyme concentration is 30-fold dilute compared to typical cryoEM conditions and the 2-decameric fraction significantly decomposed into decamer, as assessed by mass photometry (sSupplementary Figure 14A). Upon increasing enzyme concentration to 0.1 mg/mL, which is within the range of our cryoEM experiments (0.3 mg/mL for all datasets except where indicated) and shown to support filamentation by chemical crosslinking (Figure 1D), we uncovered a subtle, 2-fold $K_{M,\ ammonia}$defect for the 2-decamer fraction compared to the decamer fraction for wild-type GS (Supplementary Figure 14B).

To probe this defect in K_M further, we took the decameric fraction at 0.1 mg/mL and repeated steady-state assays in the presence or absence of the glutamine concentration used to stabilize filamentation by CryoEM (Supplementary Figure 15). The presence of glutamine increased $K_{M,\ ammonia}$ three-fold for WT, but had smaller effects for the mutations at the interface that directly interact with the ligand (Figure 2F). Given the incomplete filament formation observed in our cryoEM experiments, with a maximum filament formation of ~50% at 0.3 mg/mL concentration (Supplementary Figure 9), the effective $K_{M,\ ammonia}$ defect upon filamentation is likely at least 2-fold higher than measured. The range of $K_{M,\ ammonia}$ values reported here are near the ammonia concentration estimates reported in the blood and liver under normal physiological conditions (<50 μM) and lower than hyperammonemic conditions (0.2 - 1 mM) (Albe et al. 1990; Dasarathy et al. 2017).

The filament state impacts conformational variability of E305-loop

To understand the structural basis underlying the $K_{M,\ ammonia}$ defect, we inspected the interactions of active site residues and loops for differences across the oligomeric forms of GS. The GS active site forms a bifunnel shape with ATP gaining access to one subsite with glutamate and ammonia accessing the other subsite (Figure 3A). The glutamate/ammonia binding site is gated by a flexible loop that bears two key catalytic residues: R299, which interacts with glutamate substrate carboxyl group, and E305, which is predicted to deprotonate ammonium ions to ammonia, enabling the required nucleophilic attack of the y-glutamyl phosphate intermediate (Owji et al. 2022; Krajewski et al. 2008). Previously, crystal structures of human GS revealed a closed loop conformation in the presence of the transition state inhibitor methionine sulfoximine (PDB 2QC8). However, this loop exhibited weak electron density in the ADP-bound state (PDB 2OJW), which potentially indicates mobility of this element throughout the catalytic cycle.

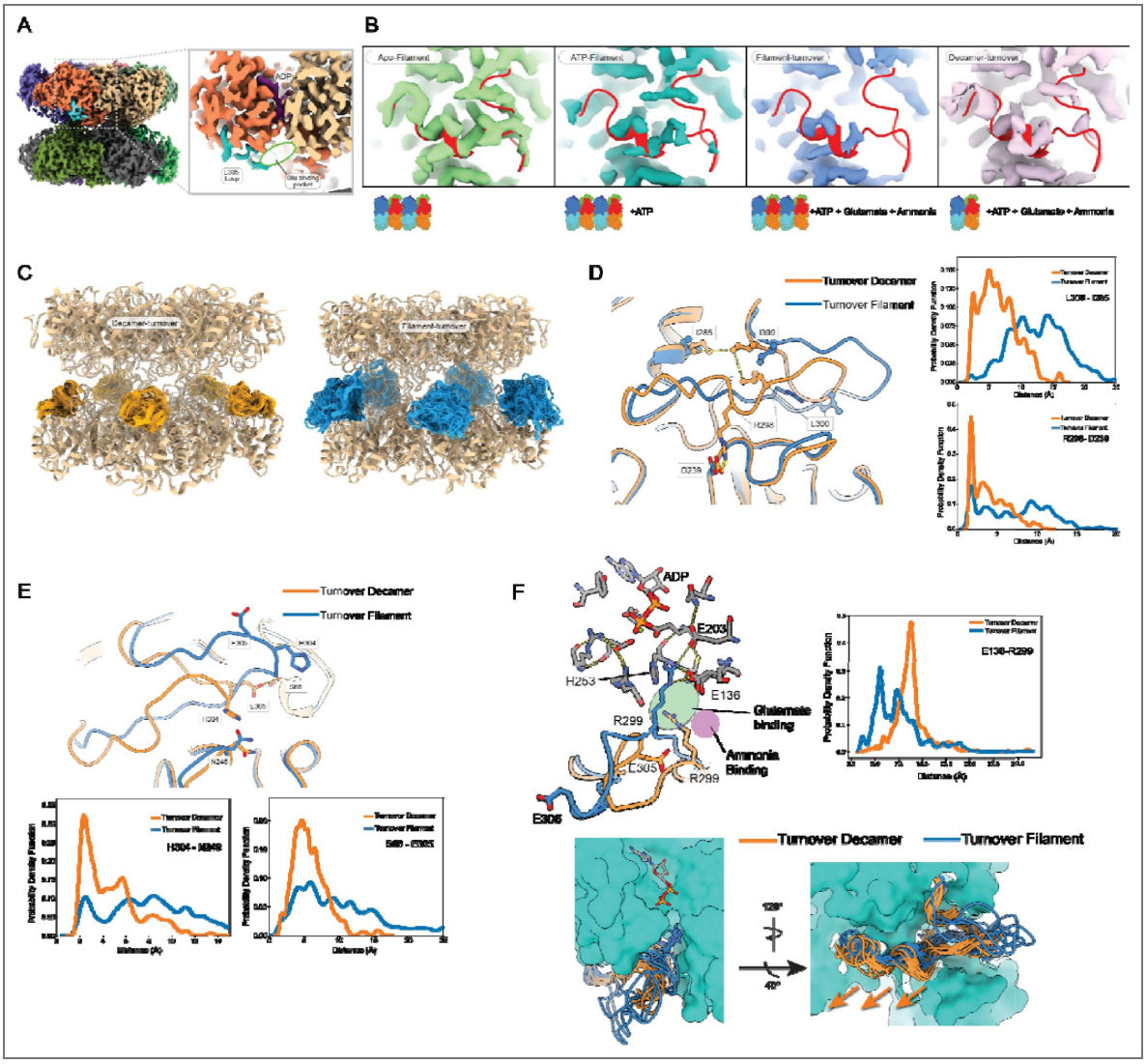

Figure 3. Variable E305-loop density and conformations in human glutamine synthetase.

A) Turnover-decamer cryoEM density map is colored based on monomer except for one E-305 loop with is colored cyan and ADP density that is colored purple demonstrating how the E305-loop closes over the active site to enclose the glutamate and ammonia binding site. B) CryoEM E305-loop density representations for the apo-filament, ATP-filament, turnover-filament, and turnover-decamer maps with 2QC8 docked into each map shown in red. The contour is chosen to equalize the relative density levels in other regions of the protein (**Supplementary** Figure 16). C) Representation of EMMIVox ensembles of the E305-loop (residues 295-309) for one pentamer (decamer-orange and filament-blue) overlaid with ribbon structure of consensus model (tan). (D) Single filament and decamer turnover monomers overlaid and presented in blue and orange respectively presenting a hydrophobic stabilizing patch (I285, L300, and I309) and stabilizing salt-bridge (D239 and R298) in the 'closed active' loop state that is missing in the filament models. Distance measurements calculated across full EMMIVox ensembles represented as kernel density function between residues participating in 'closed active' loop state are presented demonstrating bias away from these contacts in the turnover filament form. (E) Same as (D) but representing the 'tip' of the loop showing E305 hydrogen bonding with S66 and H304 hydrogen bonding with N246 with quantification of these distances from the ensemble. In all cases, the filament oligomeric state under turnover conditions disfavored these interactions. (F) MD-refinement of the cryoEM filament turnover map revealed active site loop infiltration into the active site with R299 hydrogen bonding with active site residues E136 (top left) with distance quantification of R299 to E136 in the active site (top right). At bottom, overlay of all ten monomers per MD-refined model with loops in ribbon, ADP in stick, and the rest of the model is represented in surface. The filament loop is in an outward conformation from the active site at the base of helix 8.

Given the importance of this loop in gating glutamate and ammonia access to the active site, we examined how the E305-loop conformation and dynamics varied upon filament formation and substrate identity. All maps had similar resolution range ($FSC_{0.143}$ between 1.95 - 2.27Å, Supplementary Figure 3, Supplementary Figure 4, Supplementary Figure 8, Supplementary Figure 12) and showed defined secondary structure and amino acid side chains in helix-12 (266-288) and beta sheet-11 (313-316) on either side of the loop at similar density contours (Supplementary Figure 16). The apo-filament cryoEM map showed well resolved density for the E305-loop with clear side chains, which support building an atomic model in a conformation we call the "closed-active state" (Figure 3B). Loop conformational heterogeneity was also influenced by nucleotide state, as the filament map with ATP only displayed partial density (Figure 3B). By contrast, the filament map collected during turnover displayed almost no density in the region, which is indicative of a greater degree of disorder. However, the E305-loop was partially restored in the cryoEM map of the turnover-decamer map (Figure 3B). The differential loop density between turnover-decamer and turnover-filament species was further supported by 3D classification of symmetry-expanded particles, which recovered partial E305-loop density in 4/12 turnover-decamer classes (C5; Supplementary Figure 18) compared to 0/12 classes for the turnover-filament (D5; Supplementary Figure 19). This observation implicates the E305-loop conformational distribution as a potential factor contributing to the observed impaired kinetics of GS filaments. Taken together the E305-loop is sensitive to nucleotide state and also by filament state under turnover conditions.

The changes in density for the loop results from conformational heterogeneity that is 'averaged out' upon reconstruction. To provide an atomistic model of the conformational space explored by the E305-loop, we used Bayesian inference to balance experimental cryoEM data with accurate physico-chemical molecular dynamics as implemented in EMMIVox ensemble refinement (Hoff et al. 2024). Across different conditions, the conformation of the loop was dominated by the closed-active loop conformation (Figure 3C). However, the turnover-filament model displays distended loop conformations diverged from the active-closed state that we turn collectively as the 'open ensemble' of loop conformations (Figure 3C). The E305-loop (residues 299 - 311) sampled a more diverse ensemble (with root mean square fluctuation values of greater than 10Å) in the turnover filament state, with the turnover decamer and apo-filament displaying reduced variability (Supplementary Figure 17). By contrast, across all states, the remainder of the active site maintained similar fluctuations (Supplementary Figure 17).

We next examined the principal contacts that serve to stabilize the 'active closed' state of the loop (Figure 3D,E). We observe multiple residue contacts that appear stabilizing including a hydrophobic pocket formed by L300, I285, and I309, a salt-bridge formed between R298 and D239, and a hydrogen bond between H304 and N249 (Figure 3D,E). All these interactions displayed favored distances in the decamer-turnover compared to filament turnover ensembles. A major consequence of this increased loop mobility is that Arg299 can "invade" the active site (Figure 3F). We quantified the distance distribution between R299 and E136 in our turnover-decamer and turnover-filament ensembles and found a substantial bias towards R299 infiltration of the active site in the filament ensemble that is absent in the turnover decamer ensemble (Figure 3F). The conformation of Arg299 could potentially sterically hinder substrate access to the active site and thus contribute synergistically with loop mobility to the observed $K_{M,\ ammonia}$ defect. Collectively, these results suggest that biasing of conformational distribution of the loop is important for tuning activity in GS.

Global conformational change coordinates E305-loop dynamics

We next asked what conformations or structural features underlie these changes to E305-loop conformational space and how filament formation promotes an 'open ensemble'.

Utilizing our EMMIVox refined models as a starting point, we assessed global conformational changes between the turnover-filament and turnover-decamer structures that might influence the local conformation of the loop. First, we found a rotational conformational change (1.2°) apparent about the pentamer-pentamer interface (sFigure 4A). Given that this conformational change

could impact the local conformation at each composite active site by altering monomeric interfaces we explored how this global conformational change related to the overall conformation of each monomer. We observed a 'crimping' conformational change per monomer where in the filament structure the β-grasp domain and the catalytic domain are rotated towards each other and away from their respective active sites (Figure 4A).

We next sought to define the regions within each monomer most altered upon filament formation by performing a Cα-distance matrix subtraction analysis (Figure 4B; Supplementary Figure 20). As expected, the E305-loop conformational heterogeneity dominated this analysis, however, we also observed an ~2Å shift in the tip of the β-grasp domain (residues 70-76) and helix-8 which abuts the active site and immediately precedes the E305-loop (Figure 4B; Supplementary Figure 20). We found the largest Cα-distance change between these two regions, specifically, between N74 and E263 displaying a distance change of 2.05Å (Figure 4A). Finally, to understand how prevalent this global conformational change is we quantified this Cα-distance in the full turnover-filament and turnover-decamer ensembles and found persistent distance distribution changes of ~2Å between these two ensembles (Figure 4C). Thus, we propose that this global conformational change serves to influence E305-loop conformational distribution via two primary mechanisms via helix 8 repositioning away from the active site in the filament form which: 1) hinders E305-loop ability to completely close over the ammonia binding site (residues S66, S67, and D76;(Figure 4B,C) and 2) disfavors E305-loop contacting closed-state stabilizing residues (Figure 3D,E).

E305-loop conformational space is crucial for Michaelis-complex formation

Since all ensembles, including the apo-filament, could sample both the 'active closed' and 'open-ensemble' states, we next pursued mutagenesis to more directly test the importance of the loop flexibility on catalysis. We created alanine mutants of residues D239, R298, L300, I309, H304, and E305. Each of these residues reside on the E305-loop with the exception of D239 which participates in a salt-bridge interaction with R298 on the loop. E305 was chosen to be an active site control, which does not appear to stabilize the closed state of the loop, but rather, the closed state of the loop positions E305 near the proposed ammonia binding site (Moreira et al. 2017; Issoglio et al. 2016; Frieg et al. 2016).

We measured the steady-state Michaelis-Menten parameters of all variants (Figure 5A). The E305A variant principally impacted $K_{M,\ ammonia}$ (~10 fold) as would be expected from this residue's predicted role of deprotonating ammonium ions in preparation for nucleophilic attack. The E305A variant was also the only variant to display a large k_{cat} effect (~10 fold) which is also expected given its presumed role in priming ammonium to ammonia in the active site (Moreira et al. 2017; Issoglio et al. 2016; Frieg et al. 2016). The $K_{M,\ ammonia}$ parameter was also impacted for all other loop variants tested by 2-10 fold. However, the principal kinetic impact for other loop variants was on the $K_{M,\ glutamate}$. The magnitude of $K_{M,\ glutamate}$ change ranged from 100 fold in L300A to 5 fold in H304A. Disruption of the hydrophobic interface of L300, I309, and I285 appeared to have largest impact on $K_{M,\ glutamate}$, followed by disruption of the R298*D239 salt bridge (50-fold change for both variants), followed lastly by disruption of the H304*N249 hydrogen bond.

The $K_{M,\ ammonia}$ was impacted but generally less so than $K_{M,\ glutamate}$ in E305-loop variants. This result likely due to the use of saturating glutamate concentrations required to estimate $K_{M,\ ammonia}$ where the majority of active sites are glutamate bound, or y-glutamyl phosphate formed, which will have had already promoted the closed-active loop state via amino acid carboxylate-R299 interaction, thus restricting the potential scope of loop conformational variability. Even with such a presumed stabilization, the full Michaelis-complex formation is still impacted for the final ammonia substrate binding which is likely a consequence of the biased conformational state of the E305-loop. Taken together, these data indicate that mutations outside the active site to the E305-loop stabilizing interactions have large impacts to the K_M for substrates that bind to half-active

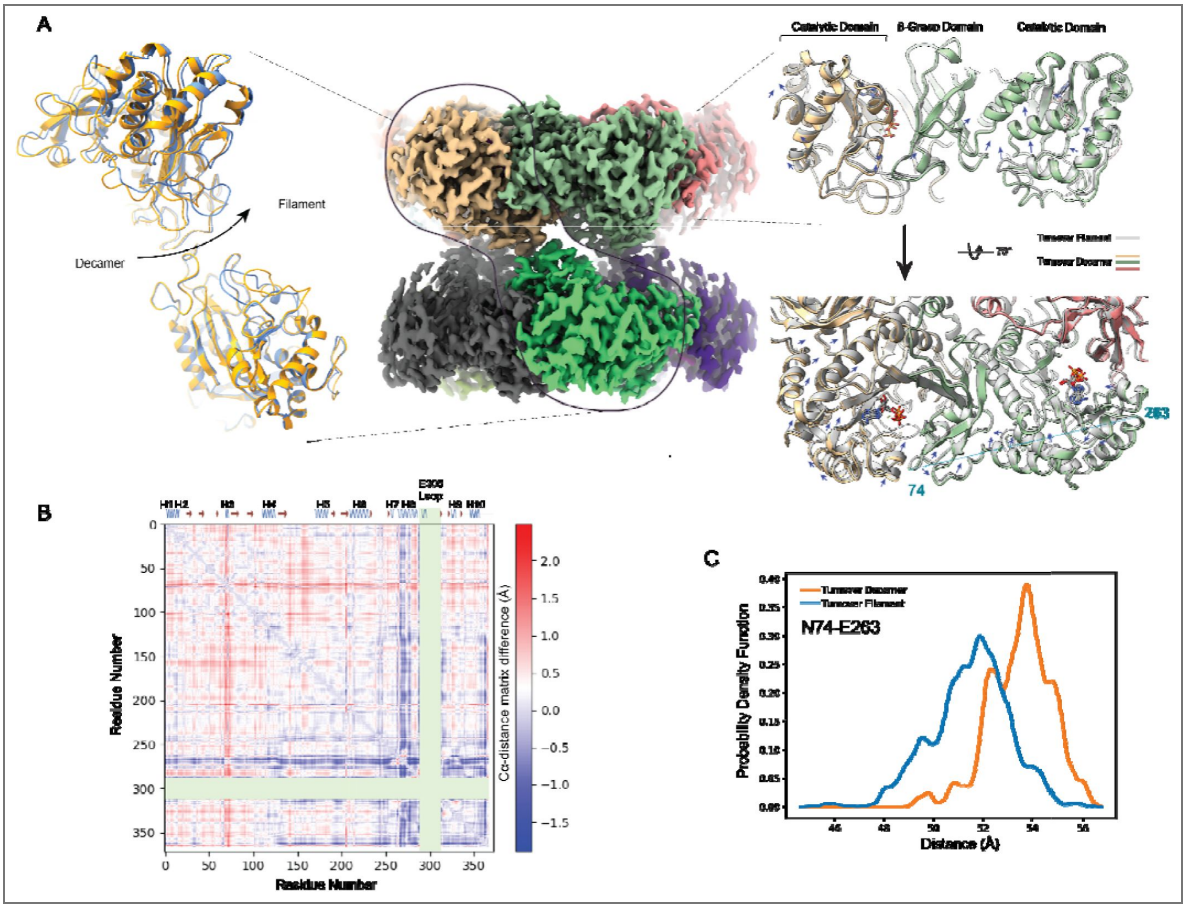

Figure 4. Global conformational change is associated with loop conformational heterogeneity under turnover conditions.

(A) Left: rotational motion about the pentameric interface observed where models were aligned on the bottom monomer and rotation seen in the upper monomer is noted (decamer in yellow and filament in blue). Middle: representation of the decameric turnover cryoEM map colored per monomer with outlines showing relevant areas shown at left and right. Right: monomeric interface within a pentamer overlay of the turnover filament model (gray) with turnover decamer model colored by monomer (tan, green, and red). Ligands are colored by atom type. Arrows indicate conformational change from filament to decamer state. The largest Ca distance change not including the E305-loop is indicated between residues 74 and 263 from across the pentamer. (B) Ca distance difference matrix for chain G between turnover decamer and turnover filament models with the E305-loop (residues 289-312) and the far C-terminal peptide (369-373) omitted with a cartoon secondary structure representation of a monomer on top and distance color legend at right demonstrating that the tip of the B-grasp region (60-76) and helix 8 (residues 262-282) showing the largest conformational differences. (C) Ca distance differences for residues 74 and 263 between the turnover filament and turnover decamer ensembles demonstrating a robust 2 angstrom distance difference.

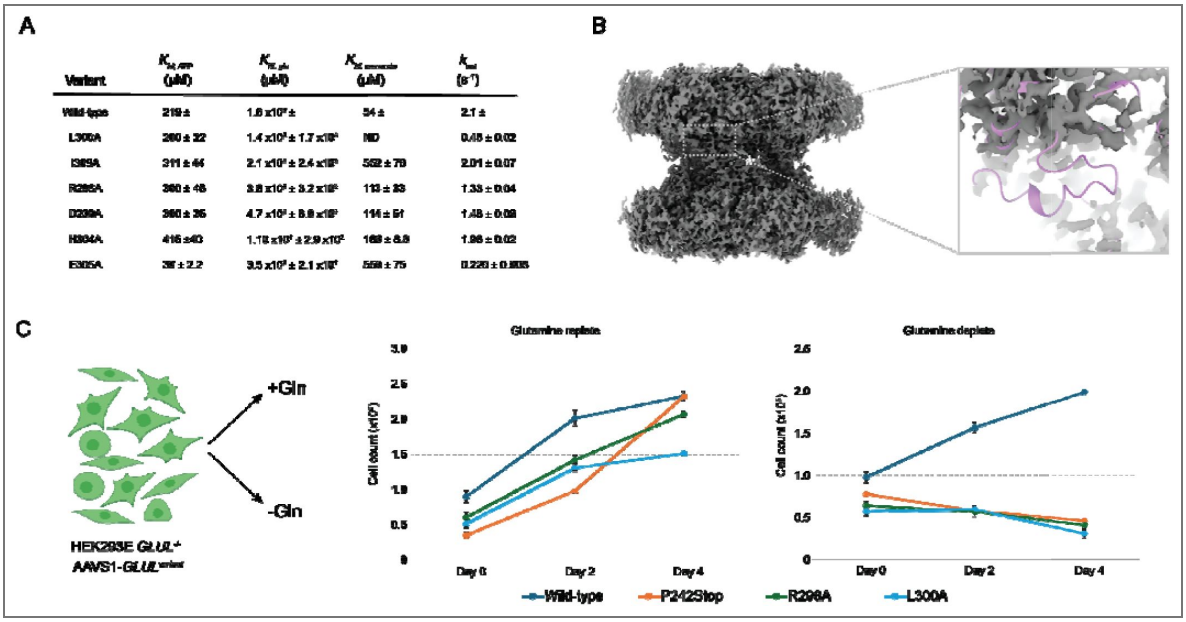

Figure 5. Glutamine synthetase E305-loop conformation controls Michaelis-complex formation.

A) Steady-state kinetic parameters for wild-type GS (also displayed in Figure 2) and six point-mutants of GS, L300A, I309A, R298A, D239A, H304A, E305A as assessed by the coupled-ADP release assay (methods). (B) cryoEM density map for R298A decamer under turnover conditions displayed in full (left) with inset focused on loop density (right) demonstrating complete loss of the E305-loop for this variant. (C) Schematic of *HEK293E GLUL-/-* cell line auxotrophic for glutamine is reconstituted with single genomic integration of individual *GLUL* variants (methods) and used to assess glutamine prototrophy. All variant cell lines grow equivalently in glutamine replete media conditions (middle) but only the wild-type *GLUL* variant could support cell growth and survival under glutamine deplete conditions, whereas R298A, L300A, and a premature stop codon at P242 all led to cell death.

sites gated by the loop. These mutations do not have pronounced effects to the overall k_{cat} however, indicating that while Michaelis-complex formation is hindered, the rate-limiting step of catalysis is unimpacted.

To test the model that loop biasing impacts K_M values for GS, we structurally characterized the decameric form of loop variant R298A under turnover conditions. The final reconstruction yielded an overall map of $FSC_{0.143}$ of 1.95 Å with high local resolution values across the map (Supplementary Figure 21). Importantly, this map, despite being the highest global resolution map reconstructed, did not display any appreciable E305-loop density (Figure 5), similar to the turnover filament (Figure 3B). Thus, the R298A mutant, even in the decameric form, would rarely adopt the active-closed conformation, explaining the $K_{M,\ glutamate}$ and $K_{M,\ ammonia}$ defects resulting from this mutation. Collectively, these data suggest a connection between loop ensemble and catalytic activity for human GS that is principally manifested in $K_{M,}$changes for amino acid and ammonium substrates.

Loop variants are unable to support glutamine auxotrophy

Since our data suggested that altering loop dynamics via mutation or filamentation could alter K_M, we next wanted to test the effect of perturbing the loop on the overall cellular activity of GS. Most human cells require exogenous glutamine to support growth in tissue culture unless they express GS. Indeed, GS expression has been used as an auxotrophic marker for antibody production HEK293E GLUL-/- cell line (Yu et al. 2018). Starting from this auxotrophic HEK293E GLUL -/- cell line, we used CRISPR to introduce an attP landing pad (Matreyek et al. 2017, 2020), to facilitate stable cell line generation expressing individual GS variants. To create each mutant line, we transfected with Bxb1 and cognate attB GLUL variant DNA. GS variants were then overexpressed from a pTet promoter driven by doxycycline and tested for growth in the presence and absence of glutamine supplementation (Figure 5C)

Glutamine prototrophy of this cell line was confirmed as high cell proliferation was observed for wild-type GS in glutamine deplete media while there was a lack of survival for a variant bearing a premature stop codon inserted at P242 (Figure 5C). We assessed glutamine auxotrophy for GS filament interface variants C53A and K52A (Supplementary Figure 23). As expected, in the HEK293 model, both variants supported glutamine auxotrophy to similar levels as wild-type. This system is not likely to be sensitive to the feedback inhibition mediated by filamentation to reduce glutamine production as ammonia levels in HEK293 cells typically exceed those levels seen in healthy tissues by up to 100-fold (Rajendra et al. 2011). However, the two loop mutants, R298A and L300A, could not support growth under glutamine-deplete conditions displaying the same phenotype as P242stop. The $K_{M,\ glutamate}$for R298A and L300A are outside the normal steady state concentrations of intracellular glutamate, suggesting that loop conformational control of the Michaelis-complex can occur in the cell to directly impact metabolic flux through GS.

Discussion

We propose a model for glutamine synthetase regulation through filament formation that alters the conformational landscape of the active site gating E305-loop (Figure 6). We show that filament formation is driven both by higher enzyme concentrations and glutamine binding at the filament interface. While the enzyme concentrations to achieve robust filamentation in the absence of glutamine are much higher than observed in cells, the protein concentrations used in our time-resolved cryoEM experiments where filamentation is correlated with accumulation of glutamine are within the range of intracellular GS concentrations in S. cerevisiae (Engel et al. 2025) and human cell lines (Wiśniewski et al. 2014). Additionally, we found that physiological concentrations of glutamine can stabilize filamentous GS structures.

GS is an ancient enzyme that is found in all domains of life as it serves a critical crossroads between carbon and nitrogen metabolism. Given its centrality to numerous metabolic pathways, GS is subject to sophisticated intracellular regulation across the domains of life. E305-loop flexibility has been noted in X-ray crystallographic structures of human GS (Krajewski et al.

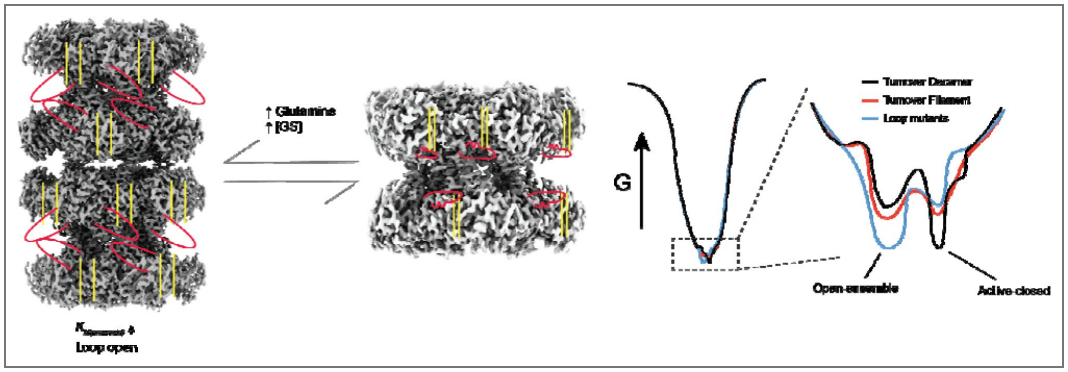

Figure 6. **Filament formation tunes E305-loop dynamics to modulate enzyme activity.**

Left: cryoEM map of the turnover filament which includes a higher $K_{M,\ ammonia}$ and open E305-loop indicated at bottom and by an 'open' red colored E305-loop cartoon. Also indicated is the global conformational change that opens up the monomeric interfaces about the active site (yellow lines). This form of the enzyme is increased with increased GS concentration and/or glutamine concentration and is different from the decamer which includes a more closed active site and less conformationally heterogeneous E305-loop. Right: proposed conformational landscape of GS wherein the global fold of the enzyme is largely retained and subtle conformational/ensemble changes found in the low thermodynamic basin are present. Inset: the E305-loop ensemble is depicted for the turnover decamer, turnover filament, and E305-loop mutants wherein the decamer slightly favors an active-closed state, the filament an open-ensemble, and loop variants significantly favor the open-ensemble state.

2008) and in other homologs too (Tecson et al. 2025) supporting a model of functional flexibility of this structural element. The most well studied is type I-beta GS (GSIB) found in gram negative bacteria which contains a 'regulatory loop' that abuts the E305-loop at the active site. The regulatory loop can be covalently adenylated by a bifunctional enzyme that is sensitive to glutamine levels and adenylation inhibits GS (Eisenberg et al. 2000).

Given our demonstration of the importance of maintaining optimal E305-loop flexibility in human GS, it is perhaps unsurprising that a large post-translational modification applied to a regulatory loop of GSIB could have a dramatic functional impact. The E305-loop thus is likely a hotspot for GS regulation via multiple distinct routes across evolution.

Here, we observe a connection between the filamentation and E305-loop flexibility. There is evidence that GS homologs from bacteria, archaea, and eukaryotes also form a filamentous, head-on-head structure, but their structural and functional consequences are incompletely understood. In E. coli, GS filaments could be formed from supraphysiological levels of select divalent cations that are chelated by adjacent helices across repeating dodecamer units.

While high structural resolution was achieved, the catalytic and cellular consequences of filament formation were not explored. Furthermore, E. coli filaments dissolved under turnover conditions leaving the functional relevance unclear. By contrast, in S. cerevisiae, GS filaments were demonstrated to negatively regulate GS activity in the cell and shown to be a crucial adaptation upon starvation conditions (Petrovska et al. 2014). Here, we provide a structural rationale describing how filament formation, stabilized by product, can structurally alter GS E305-loop to tune the substrate-limiting Michaelis constant for ammonia.

Importantly, point mutations of the interfacial residues do not show a $K_{M,ammonia}$ defect in the presence of glutamine, indicative of the importance of the filament form for product feedback. Thus, the glutamine stabilized filament formation model for human GS represents a new mode of product-based allosteric feedback inhibition for this enzyme class.

Human GS is expressed in many tissues to serve different metabolic needs. Translation and subsequent degradation of GS can take multiple hours to achieve robust expression changes (Arad et al. 1976; Van Nguyen et al. 2016, 2017; Van Nguyen 2021; Zhao et al. 2025) which is potentially insufficient to meet the changing metabolic needs of a given cell. Therefore, regulated enzyme activity through filament formation represents a mode of high temporal control over enzyme activity as it is not reliant on transcription, translation, or degradation of enzymes. Additionally, the Michaelis constant for ammonia report herein (57 μM for decameric GS and 170 μM for filamentous GS) corresponds closely to the concentrations of ammonia measured in cells, which suggests that this modulation of GS activity could have an immediate impact on intracellular turnover rates.

Moreover, our observations support the concept that allostery operates through ensemble redistribution rather than through discrete conformational switches. The filament state of human GS does not simply toggle the E305-loop between rigidly defined "open" and "closed" states, but rather shifts the probability distribution across a spectrum of conformations that collectively impact enzyme activity. This is similar to observations in IMPDH2 and PRPS filaments (Hvorecny et al. 2023; Johnson and Kollman 2020), where assembly modulates the conformational landscape accessible to regulatory elements. Both loop dynamics and filamentation are frequently implicated in tuning activity of enzymes; here a product feedback mechanism links these two concepts together. Collectively, the filament formation of human GS described here is a complex manifestation of ensemble-based allostery to enable timely regulation of enzyme activity.

Methods

Expression and purification of scarless human glutamine synthetase

An expression vector for a 6xHIS-conjugated human glutamine synthetase was ordered from ATUM. The vector was transformed into BL21(DE3) *E. coli* cells and grown overnight at 37 °C in Luria broth with 100 μg ml^{-1} carbenicillin. 5 mL of this starter culture was added to 1 L of the same medium and allowed to grow at 37 °C until an OD600 of 0.6-0.8 was reached. At this point, expression of GS was induced with 0.5 mM IPTG and the temperature was reduced to 18 °C for 16 - 18 hours. The cells were harvested by centrifugation at 4500 rpm for 15 minutes at 4 °C. The cell pellets were transferred to a 50-mL conical tube and stored at −80 °C.

For purification, cells were thawed and resuspended in 60 mM HEPES pH 7.6, 50 mM NaCl, 50 mM $MgSO_4$, 0.5 mM TCEP, 10% glycerol followed by lysis by sonication. Lysate was clarified by centrifugation and loaded onto HisTrap FF 5 mL (Cytiva) columns using a peristaltic pump, washed with 60 mM HEPES pH 7.6, 50 mM NaCl, 50 mM $MgSO_4$, 0.5 mM TCEP, 10% glycerol, 25 mM imidazole, and eluted with 60 mM HEPES pH 7.6, 50 mM NaCl, 50 mM $MgSO_4$, 0.5 mM TCEP, 10% glycerol, 250 mM imidazole. Eluate was concentrated before being aliquoted and flash frozen and stored at −80°C. Thawed aliquots were loaded onto a Superose 6 10/300 column preequilibrated with 60 mM HEPES pH 7.6, 50 mM NaCl, 50 mM $MgSO_4$, 0.5 mM TCEP and assayed for activity immediately after size-exclusion chromatography.

Expression and purification of scarless human glutamine synthetase

Scarless human glutamine synthetase was produced by either of two independent methods: N-terminal His-SUMO tagging with Ulp1 cleavage or C-terminal intein-chitin binding domain-His with DTT induced self cleavage. Both purification methods yielded highly functional GS, however, better yields were obtained via the His-SUMO tagging approach.

Human glutamine synthetase was codon optimized for E. coli (ATUM biosciences) and appended with a C-terminal Mxe GyrA intein domain (NEB IMPACT) followed by a chitin-binding domain (CBD) from *Bacillus circulans* (NEB IMPACT) cloned in-frame with a 3' His_6-tag and transformed into BL21(DE3) (NEB). Two liters of Terrific Broth (Fisher) were pre-warmed to 37L°C before being inoculated with 10Lml overnight starter culture. Cultures were grown to 0.6L<LOD600L<L1.0 and induced with 0.5LmM isopropyl β-D-1-thiogalactopyranoside (GoldBio) and protein expression was allowed to continue for 3 hours. Cells were pelleted at 3,500Lr.c.f. for 20Lmin at 4L°C, resuspended in base buffer (60 mM HEPES pH 7.6, 50 mM NaCl, 50 mM KCl, 10 mM $MgCl_2$, 0.5 mM TCEP) supplemented with 2 mg/mL lysozyme, benzonase, and cOmplete™, EDTA-free Protease Inhibitor Cocktail (Roche) and stored at −80°C until purification.

For the purification of GS-intein-CBD-His, cells were thawed and lysed by sonication. Lysate was clarified by centrifugation and loaded onto HisTrap FF 5 mL (Cytiva) columns using a peristaltic pump, washed with base NiA buffer (60 mM HEPES pH 7.6, 50 mM NaCl, 50 mM KCl, 10 mM $MgCl_2$, 25 mM imidazole), and eluted with base NiB buffer (60 mM HEPES pH 7.6, 50 mM NaCl, 50 mM KCl, 10 mM $MgCl_2$, 250 mM imidazole). Eluates were spiked with DTT to a final concentration 100 mM and stored overnight at 4°C to allow for intein self-cleavage. Cleaved GS was buffer exchanged into NiA buffer via application to a HiTrap 26/10 Desalting column (Cytiva). His_6-tagged Mxe GyrA intein-CBD was removed through an ortho NiNTA where sample was applied to a HisTrap High Performance 5 mL column (Cytiva) and the flow through fraction was collected, concentrated in an Amicon 30k MWCO centrifugal filter, spiked with glycerol to a final concentration of 10%, aliquoted, and flash frozen for long term storage at −80°C.

Human glutamine synthetase was codon optimized for E. coli (ATUM biosciences) and subcloned into a pET29a vector bearing an inframe 5' His_6-SUMO tag and transformed into BL21(DE3). Two liters of Terrific Broth (Fisher) were pre-warmed to 37L°C before being inoculated with 10Lml

overnight starter culture. Cultures were grown to 0.6L<LOD600L<L1.0 and induced with 0.5LmM isopropyl β-D-1-thiogalactopyranoside (GoldBio) and protein expression was allowed to continue for 3 hours. Cells were pelleted at 3,500Lr.c.f. for 20Lmin at 4L°C, resuspended in base buffer (60 mM HEPES pH 7.6, 50 mM NaCl, 50 mM KCl, 10 mM $MgCl_2$, 0.5 mM TCEP) supplemented with 2 mg/mL lysozyme, benzonase, and cOmplete™, EDTA-free Protease Inhibitor Cocktail (Roche) and stored at −80°C until purification.

For the purification of His_6-SUMO-GS, cells were thawed and lysed by sonication. Lysate was clarified by centrifugation and loaded onto HisTrap FF 5 mL (Cytiva) columns using an AKTA start, washed with base NiA buffer (60 mM HEPES pH 7.6, 50 mM NaCl, 50 mM KCl, 10 mM $MgCl^2$, 25 mM imidazole; 250 mL), and eluted with base NiB buffer (60 mM HEPES pH 7.6, 50 mM NaCl, 50 mM KCl, 10 mM $MgCl^2$, 250 mM imidazole; 50 mL).

Eluates were spiked with Ulp1 (see purification below) and dialyzed overnight at 4°C against base buffer. Cleaved GS was separated from His_6-tagged His-SUMO through an ortho NiNTA where sample was applied to a HisTrap High Performance 5 mL column (Cytiva) and where scarless GS could elute with application of base buffer with 25 mM imidazole. Scarless GS was concentrated in an Amicon 30k MWCO centrifugal filter, spiked with glycerol to a final concentration of 10%, aliquoted, and flash frozen for long term storage at −80°C.

Prior to experimentation, a scarless GS aliquot was thawed, filtered through a 0.22 μm filter, and applied to a Superose 6 increase 10/300 size-exclusion column pre-equilibrated with base buffer. Unless otherwise stated, the decameric peak corresponding to a 16 mL retention volume was collected and stored at 4°C throughout the duration of experimentation. Activity of this peak was unchanged for up to 2 weeks and all biochemical experiments were performed immediately upon purification.

Purification of Ulp1 Sumo protease

The expression vector encoding His_6-Ulp1 protease was a gift from the Verba lab at UCSF obtained originally from Addgene 64697. Ulp1 was expressed and purified as previously described (Guerrero et al. 2015) with minor adaptations detailed below. Briefly, 2L of Terrific broth were pre warmed to 37°C before inoculation with 10 mL of a starter culture of BL21(DE3) cells bearing the His_6-Ulp1 expression vector. Cells were grown to $0.6 < OD_{600} < 0.8$ before temperature was dropped to 20°C and expression was induced with 0.5 mM IPTG overnight. Cells were pelleted at 3,500Lr.c.f. for 15 min at 4°C and stored in a 50 mL tube at −80°C until preparation.

Cells were resuspended in Lysis buffer (50 mM HEPES pH 8, 350 mM NaCl, 0.5 mM TCEP, 10 mM imidazole, 2 mg/mL lysozyme, benzonase, and cOmplete™ EDTA-free Protease Inhibitor Cocktail (Roche). Lysate was clarified by centrifugation and loaded onto HisTrap FF 5 mL (Cytiva) columns using an AKTA start, washed with 25 mL of Lysis buffer followed by 25 mL of Buffer A (50 mM HEPES pH 8, 350 mM NaCl, 0.5 mM TCEP, 10 mM imidazole) and 25mL of Buffer B (50 mM HEPES pH 8, 350 mM NaCl, 0.5 mM TCEP, 30 mM imidazole). Finally Ulp1 was eluted with 25 mL of Buffer C (50 mM HEPES pH 8, 200 mM NaCl, 0.5 mM TCEP, 300 mM imidazole). Pure fractions were combined and dialyzed against 50 mM HEPES pH 8, 200 mM NaCl, 10 mM EDTA, 0.5 mM TCEP, 20% glycerol). Ulp1 was concentrated to 2 mg/mL and flash frozen in 250 μL aliquots and stored at −80°C.

Negative stain microscopy

GS was prepared to ~0.01 - 0.05 mg/mL in base buffer prior to application to glow-discharged carbon-coated grids, stained with 0.7% uranyl formate and imaged on a T12 (FEI) operating at 120LkV. Images were acquired at ×57,000 magnification on a Gatan Rio camera. Two-dimensional classification and averaging was conducted using cisTEM.

BSG and BMOE crosslinking of GS filament interface

BMOE (bismaleimidoethane; ThermoFisher) and BSG (bis(sulfosuccinimidyl) glutarate-d0; ThermoFisher) powder was thawed to room temperature and reconstituted in DMF to a concentration of 50 mM, aliquoted, flash frozen in liquid nitrogen, and stored at −80°C. Protein samples were diluted to concentrations noted in base buffer (60 mM HEPES pH 7.6, 50 mM NaCl, 50 mM KCl, 10 mM $MgCl_2$, 0.1 mM TCEP) and reacted with crosslinker to a final concentration of 0.5 mM for 10 mins at room temperature followed by quench in 5X SDS-PAGE sample buffer (225 mM Tris pH 6.8, 50% glycerol, 0.05 % SDS, 0.2 mg/mL bromophenol blue, 1M DTT) supplemented with 100 mM NH_4Cl to quench BSG reactions only. Protein concentrations were normalized after quench prior to SDS-PAGE analysis.

Michaelis-Menten analysis using coupled ATPase assay

ATP-hydrolysis rates were determined using an NADH-coupled assay (pyruvate kinase and lactate dehydrogenase; Sigma) as described previously (Shapiro and Stadtman 1970). Stocks of ATP, NADH, and phosphoenolpyruvate were made in base buffer (60 mM HEPES pH 7.6, 50 mM NaCl, 50 mM KCl, 10 mM $MgCl_2$, 0.5 mM TCEP) and the pH was adjusted until it reached 7.5 on ice prior to aliquoting, flash freezing, and storage at −80°C in the dark. NADH was only exposed to light upon thawing and assay set up and no appreciable change in absorbance of control experiments were noted. Briefly, GS was diluted into ATPase mix (final concentrations: 1 mM NADH, 7.5 mM phosphoenolpyruvate, 6 U/mL pyruvate kinase, and 6 U/mL lactate dehydrogenase), applied to a 384-clear bottom plate (Corning) in 10 µL final volume. Steady-state depletion of NADH was assessed by measuring the absorbance at 340 nm in a Spark 10M multimode plate reader (Tecan). Single substrate concentrations were varied under saturating conditions of other substrates as determined by primarily kinetic assessment. Solution pathlength was manually determined per experiment through titration of NADH and used to calculate ATPase rate. Resultant enzyme normalized velocities were plotted against variable substrate concentration and fit using Equation 1:

$$v_o = \frac{k_{\text{cat}} * [\text{ substrate }]}{K_M + [\text{ substrate }]} \quad (1)$$

The low concentrations of ammonium required to assess $K_{\text{M,}ammonia}$ (< 10 µM) resulted in small changes in total NADH concentration (<1%) relatively quickly and therefore use of full progress curve analysis was pursued as described(Johnson 2019), which captures the rate of substrate depletion or production formation over time as [S] decreases by fitting to the differential equations inherent to the Michaelis-Menten kinetic model. Here, saturating glutamate and ATP concent ations were used in combination with three starting ammonia concentrations (750 µM, 375 µM, and 188 µM) and the NADH-coupled assay components as above in 2X concentration before being mixed with 2X enzyme (0.1 mg/mL final) and the resultant 10 µL reactions (n = 8) were monitored for 5 mins at room temperature in a Spark 10M multimode plate reader (Tecan). Replicates were averaged and the average standard deviation per time point was imported in Kintek Explorer. A standard Michaelis-Menten model was applied to the simulation defined by k_1, k_{-1}, k_2, k_{-2}, and k_3 as defined in Equation 4.

$$E + S \underset{k_{-1}}{\overset{k_1}{\rightleftarrows}} ES \underset{k_{-2}}{\rightleftarrows} EP \xrightarrow{k_3} E + P \quad \text{Scheme 1.}$$

$$k_{cat} = \frac{k_2 k_3}{k_2 + k_{-2} + k_3} \quad (2)$$

$$K_M = \frac{(k_2 + k_{-1})(k_{-2} + k_3)}{k_1(k_2 + k_{-2} + k_3)} \quad (3)$$

$$\frac{k_{cat}}{K_M} = k_1 \frac{k_2 k_3}{k_2 k_3 + k_{-1}(k_{-2} + k_3)} \quad (4)$$

Derived elementary step parameters and their associated uncertainties were used to determine the steady state kinetic parameters with error propagated through each step. The derived k_{cat} parameters from this procedure were in agreement with those derived under the traditional initial rate procedure.

Sample preparation for cryoEM analysis

Frozen, mostly pure, GS aliquots were thawed and further purified by size-exclusion chromatography on a superose 6 10/300 column where fractions corresponding to the decamer oligomeric state (~16 mL) were collected, quantified by A_{280} and tested for activity. Grids (Quantifoil 1.2/1.3 Cu 300 (with or without +2nm C) or Quantifoil 2/2 Au 200) were glow discharged in a Pelco-Easi Glo (15 mA, 10-15s on, 10-15s off) before sample application. Enzyme (0.3-1.3 mg/mL final) in apo (buffer added) or turnover (5 mM ATP, 25 mM ammonium chloride, and 50 mM glutamate; reacted for 53-600s and within steady-state kinetic regime except for the turnover-filament dataset where near full conversion of substrate to product was expected) or ATP bound (5 mM ATP) at room temperature before application to grid held at 4° or 18°C in a Mark IV Vitrobot (ThermoFisher) prior to vitrification. For turnover conditions, all data were collected on Quantifoil 1.2/1.3 Cu 300 +2nm C grids where reactions were initiated at room temperature immediately before being applied to grid in a Vit obot Mark IV (Thermo) pre-equilibrated to 18°C with 100% humidity and allowed to adsorb to ultrathin carbon layer for 30s before blotting (blot force 3, 11s, Whatman Filter Paper #1) and plunge frozen into liquid ethane. For apo- and ATP-filament datasets, grids were held at 4°C with 100% humidity, blotted 1-3 times with sample, before plunge frozen in liquid ethane. Observation of short filamentous structures was observed with and without depositing 2nm continuous carbon film on grid and preparations

CryoEM data collection

Wild-type decamer turnover, time-resolved datasets, and R298A decamer turnover GS sample grids were loaded onto a Titan Krios G3i 300 keV microscope (TEM Gamma; SLAC S2C2 Facility, Menlo Park, CA) with a BioQuantum energy filter (20 kV) and Gatan K3 Ceta-D direct detector operating at a nominal magnification of 105,000x corresponding to a physical pixel size of 0.86 Å. A zero-loss peak optimization and gain reference was taken ahead of each data collection. Each dataset was set to a total accumulated dose rate of 40 e-/Å^2 per micrograph. Each movie was split into 75 frames and a nominal defocus range was set between −0.8 to −2.0 µm. Fringe-free illumination was utilized and image shift was used to collect multiple images within a single hole and beam tilt was adjusted to achieve coma-free alignment during image shift. Automated data acquisition was performed with EPU software.

The low resolution turnover filament dataset was collected at SLAC S2C2 Facility (Menlo Park, CA) on a Talos Arctica G2 200 keV microscope with a Gatan K3 direct detector operating at a nominal magnification of 106,000X corresponding to a physical pixel size of 0.86 Å. A zero-loss peak optimization and gain reference was taken ahead of each data collection. The dataset was set to a total accumulated dose rate of 40 e-/Å^2 per micrograph. Each movie was split into 40 frames and a nominal defocus range was set between −0.8 to −2.0 µm. Automated data acquisition was performed with EPU software.

The turnover filament dataset was collected at the UCSF CryoEM Core facility where grids were loaded onto a Titan Krios G2 300 keV microscope (Krios 1) with a 20kV energy filter and Gatan K3 direct detector operating at a nominal magnification of 106,000x corresponding to a physical pixel size of 0.82 Å. A zero-loss peak optimization and gain reference was taken by facility management each week. Total accumulated dose rate of 45 e-/Å^2 per micrograph. Each movie was split into 75 frames and a nominal defocus range was set between −0.8 to −2.0 µm. Fringe-free illumination was

utilized and image shift was used to collect multiple images within a single hole and beam tilt was adjusted to achieve coma-free alignment during image shift. Automated data acquisition was performed with SerialEM software.

Apo- and ATP-Filament datasets were collected at the Arnold & Mabel Beckman center for cryo-electron microscopy at the University of Washington where grids were loaded onto a Titan Krios G3 300 keV microscope (Krios 1) with a 20kV Gatan BioQuantum energy filter and Gatan K3 direct detector operating at a nominal magnification of 105,000x corresponding to a physical pixel size of 0.843 Å. Total accumulated dose rate between 60 and 64.2 e-/Å^2 per micrograph.

CryoEM image processing and model building

Movies were aligned, motion-corrected, and dose-weighted using Patch Motion Correction in cryoSPARC (v3.1 and above) or cryoSPARC Live, except for the turnover filament dataset which was motion-corrected and dose-weighted on-the-fly with MotionCor2 (v1.3.0). Contrast transfer function (CTF) estimation was performed in cryoSPARC using the Patch CTF except for the turnover filament dataset which was estimated using CTFFIND4 'on-the-fly' as part of the Scipion (v2.0) software suite. Micrographs with poor CTF fit (generally >5 Å and/or containing crystalline ice) were discarded. All further processing steps were performed in cryoSPARC (v3.1 or higher) where blob picked particles were classified in two dimensions and non-background particles were subject to either further rounds of template picking and 2D classification or used for 3D homogeneous refinement using either *ab initio* prepared input maps or using maps from other datasets as 3D refinement input. Where applicable, particles were further selected with either or a combination of heterogeneous refinement and/or 3D classification as shown in the supplemental figures. Homogeneous or non-uniform refinement was utilized for final refinement and reconstructions and typically included a symmetry operator (D5 for filament reconstructions, C5 for R298A decamer turnover reconstruction and C1 for wild-type decamer turnover reconstruction). Local map resolution was estimated in cryoSPARC for the final maps. Focused masks were generated in ChimeraX (v.1.7 and above). Focused refinement and 3D classification (3 Å filter resolution, PCA initialization) were performed in cryoSPARC. Strategy of class picking and refinement are noted in Supplementary Figure 19 and Supplementary Figure 18

An initial model, PDB 2OJW, was used to build the apo-filament model and the apo-filament model was used as the initial model for all subsequent model building. Ligands were placed with ISOLDE (v1.7) and those with >0.5 Qscore and supporting biochemical and/or literature precedent were built. Models were built iteratively using the ISOLDE (v1.7) plugin for ChimeraX (v.1.7 and above), Coot (v0.9.8.7), and Phenix (v1.20.1; Real Space Refinement and CryoEM Comprehensive Validation). Models were additionally validated with Q-score as a plugin function for ChimeraX (Supplementary Table 1). Final cryoEM maps were sharpened in Phenix using the Autosharpen feature by half-maps.

Decamer:Decamer rotation across the filament interface was determined through inspection of the apo-filament cryoEM map in ChimeraX where an outline of a pentamer from one decameric unit was rotated with respect to the outline of a pentamer across the filament interface and the rotation was depicted in Figure 1D.

MD-based cryoEM ensemble refinement

Initial models of glutamine synthetase under turnover conditions in the filament (complexed with ATP and MG) and decamer form (complexed with ADP, ATP and MG), as well as a model of glutamine synthetase in the apo-filament form generated from cryoEM data were processed using the CHARMM-GUI server to initialize molecular dynamics simulations (Jo et al. 2008). Each system was solvated in a triclinic box such that the edge of the box was 1.0 nm away from the closest atom of each glutamine synthetase model. K^+ and Cl^- salts were added to the system at a concentration of 0.15 M, along with additional ions to neutralize the charge of each system. The CHARMM36m forcefield was used for the proteins and the CHARMM General Forcefield (CGenFF) (Vanommeslaeghe et al. 2010) was used for the ATP and ADP molecules present in the turnover condition systems. Water molecules were modeled using the mTIP3P model (MacKerell et al.

1998). All simulations were carried out using a leap-frog algorithm with a 2 fs timestep. The smooth particle mesh Ewald method (Essmann et al. 1995) was used for calculating electrostatic interactions within a cutoff distance of 1.2 nm. Van der Waals interactions were gently decreased at 1.0 nm and cutoff at 1.2 nm. All simulations were performed using GROMACS v 2021.5 (Abraham et al. 2015) paired PLUMED v 2.9 (Tribello et al. 2014).

Details of EMMIVox Simulations.

Refined single-structure models and structural ensembles of the GS in the apo-filament, turnover filament, and turnover decamer forms were generated using EMMIVox (Hoff et al. 2024). In brief, EMMIVox is a Bayesian inference approach to determine single-structure models and structural ensembles from 3D cryoEM maps. The direct utilization of experimental cryoEM density and 3D half-maps in the Bayesian framework of EMMIVox automatically balances experimental information with accurate physico-chemical models. Both single structure refinement and ensemble modelling followed the standard EMMIVox protocol (Hoff et al. 2024). CryoEM maps for each GS system and their associated half-maps were pre-processed prior to EMMIVox simulations. Correlated voxels within the experimental 3D maps were removed. This was achieved by first selecting all voxels within 3.5 Å of the model and removing correlated data points with a correlation greater than a pearson coefficient threshold of 0.8. Next, the difference between voxel density for the two half-maps of each system were used to generate a lower bound for the error parameter associated with each density voxel in the EMMIVox framework. Equilibration and production simulations were performed as follows. First, each system was energy minimized using the steepest gradient descent approach. Next, a 10 ns long NPT equilibration was performed using the Bussi-Donadio-Parrinello thermostat (Bussi et al. 2007) and Berendsen barostat (Berendsen et al. 1984) set at 300K and 1 atm respectively. Next, 2 ns long NVT simulations were formed using the same thermostat at 300K. Positional restraints were applied to the NPT and NVT equilibration simulations. Next, an optimal scaling factor between the predicted and observed cryoEM maps was determined using the NVT equilibration simulation trajectory and the PLUMED *driver* tool. Scaling factor values between 0.5 and 1.8 were scanned at 0.05 intervals, with the scaling factor resulting in the lowest EMMIVox hybrid energy score selected for use in the production simulations. B-factors for each chain in the GS were optimized independently without the use of symmetry constraints.

Single-structure refinement production simulations were performed in the NVT ensemble using the thermostat conditions of the NVT equilibration run. Each GS system studied was simulated for 10 ns, with B-factor values sampled every 500 MD steps and a maximum MC move of 0.05 nm^2. To optimize performance, the EMMIVox hybrid energy was calculated every 4 MD timesteps. After single-structure refinement, the conformation with the lowest EMMIVox hybrid energy and the associated B-factor values were extracted. This structure was then energy minimized while the B-factor values were simultaneously sampled using a modified MC sampler allowing only downhill moves. Any discontinuities in the final structure obtained from the energy minimization due to the PBC were then fixed using the PLUMED *driver* tool. We then generated a PDB of the final refined structure and optimized B-factor values. These models represent the final refined single-structure models of each GS system.

EMMIVox ensemble simulations were performed using the same settings as in the single-structure refinement, with the exception of the B-factors, which were fixed, for all residues, at the lowest value obtained from single-structure refinement as a measure of background noise. 20 metainference replicas were used for each system, with each replica run for 20 ns, resulting in 400 ns of total simulation time per system.

Pairwise residue distance distributions

The probability distribution of residue-residue distances for selected residue pairs were calculated by taking the minimum distance between any two atoms within the selected residue pair for each conformation present in the structural ensemble extracted from EMMIVox. The calculation was

performed for each chain within GS, resulting in 10 residue-residue distances extracted for each conformation in the structural ensemble. Kernel density estimation plots were done using a bandwidth adjustment value equal to 1. Histograms plots were calculated using 150 bins.

Glutamine synthetase knockout HEK293e cell culture and landing pad clone generation

HEK293E glutamine synthetase knockout cells (Yu et al. 2018) and any derivatives were cultured in Dulbecco's modified Eagle's medium (DMEM; high glucose, pyruvate, with glutamine; Gibco) supplemented with 10% dialyzed fetal bovine serum (Gibco), 1x GSEM supplement (Sigma-Aldrich), and Penicillin-Streptomycin (10U Penicillin/10 µg ml^{-1}; Gibco). Cells were grown on plates at 37 °C with 5% CO_2. For routine passaging, cells were detached using trypsin–EDTA 0.25% (Gibco), resuspended in medium, centrifuged for 5 minutes at 200 x g, resuspended and plated.

Landing pad clones were generated as described previously using dAAVS1-TetBxb1BFP (Matreyek et al. 2017, 2020). Successful clones were verified by genomic PCR and co-transfection of attB-EGFP and attB-mCherry. Clone 15 passed all validation tests and was used for all following experiments (referred to in Methods as GS-KO-TetBxb1BFP and *HEK293E GLUL*$^{-/-}$ in main text). Long-term passaging of GS-KO-TetBxb1BFP was done with the addition of 2 µg ml^{-1} doxycycline (Sigma-Aldrich).

Recombination of single-variant clones or libraries into the GS-knockout-landing pad cell line

Single-variant clones were recombined into the Tet-on landing pad in GS-KO-TetBxb1BFP cell. Transfection of attB-GS variant 0.5 x 10^6 cells per well transfected with 1.5 µg attB-plasmid DNA and 1.5 µg pCAG-HA-NLS-coBxb1 using Lipofectamine 3000 (Thermo) per manufacturer recommendations. Two days post-transfection, cell media was refreshed with the addition of 2 µg ml^{-1} doxycycline. Four days post-transfection, cells were selected with media containing 2 µg ml^{-1} doxycycline (Sigma-Aldrich) and 0.25 µg ml^{-1} puromycin (Gibco). Cells were selected for one week under puromycin and the resultant stable cell lines were frozen in 10% DMSO (Sigma) in FBS (Gibco) for future experiments.

Growth test of wild type GS and disease mutants in GS-KO-TetBxb1BFP

To determine the growth rate of different glutamine synthetase variants in the presence and absence of glutamine, stable *HEK293E* $GLUL_{variant}$ cell lines (wild-type, C53A, K52A, R298A, L300A, or P242stop) were plated at low confluence (10,000 cells per well) in a series of identical white, tissue culture treated, 96-well plates (GreinerBio) in DMEM (+glutamine and 10% dialyzed FBS, GSEM, 10U Penicillin, 10 µg ml^{-1} Streptomycin, 2 µg ml^{-1} doxycycline, and 0.25 µg ml^{-1} puromycin) and allowed to adhere to the plate for 4 hours. Subsequently, media was swapped (DMEM with 10% dialyzed FBS, GSEM, 10U Penicillin, 10 µg ml^{-1} Streptomycin, 2 µg ml^{-1} doxycycline, and 0.25 µg ml^{-1} puromycin and with or without glutamine) and a Day '0' cell count time point was measured using the CellTiter-Glo kit (Promega). Following the protocol from the vendor, CellTiter-Glo reagent was mixed 1:1 ratio with cells and incubated for 10 mins at room temperature to lyse and provide a luminescence readout. Luminescence was measured on a Veritas luminometer and converted to cell counts from a standard curve of *HEK293E* $GLUL_{wild-type}$.

Data availability

Cryo-EM structures and atomic models have been deposited in the Electron Microscopy Data Bank (EMDB) and Protein Data Bank (PDB), respectively, with the following accession codes: EMD-70845, PDB: 9OTQ (Apo-Filament); EMD-70841, PDB: 9OTM (Turnover Filament); EMD-77146 (Focused Refinement Turnover Filament); EMD-70843, PDB: 9OTO (Turnover Decamer); EMD-70842, PDB:

9OTN (ATP bound Filament); EMD-70844, PDB: 9OTP (R298A turnover). Aligned and dose-weighted micrographs used to develop the turnover-filament structure (EMD-70841) are publicly available on EMPIAR (EMPIAR-13621). Initial extracted, template-picked particles from the time-resolved cryo-EM datasets are publically available on EMPIAR (EMPIAR-13622). EMMIVox ensemble refinement and trajectory files are available on Zenodo (10.5281/zenodo.2029885510.5281/zenodo.15742546). Maps emerging from focused classification or focused refinement are also available on Zenodo (10.5281/zenodo.20298855). All the GROMACS topologies and PLUMED input files needed to reproduce our EMMIVox calculations as well as the final refined single-structure models are available in PLUMED-NEST (*https://www.plumed-nest.org/*), the public repository of the PLUMED consortium (PLUMED consortium 2019), as plumID:25.017.

Acknowledgements

We acknowledge funding for ERG (F32GM144982),JSF (R35 GM145238), SEH (Pasteur-Roux-Cantarini postdoctoral fellowship), and JMK (R35 GM149542) . We acknowledge Douglas Fowler and Kenny Matreyek for providing constructs and advice for landing pad integration. The time-resolved cryoEM datasets that led to the reconstruction of the turnover-decamer and another dataset leading to the R298A turnover decamer reconstruction were collected at the S2C2 Stanford-SLAC CryoEM Center which is supported by the National Institute of General Medical Sciences (1R24GM154186). Cryo-EM equipment at UCSF is partially supported by NIH grants S10OD020054, S10OD021741 and S10OD026881 and Howard Hughes Medical Institute.

Additional files

Supplementary Material.

Additional information

Funding

Funder	Grant reference number	Author
HHS | National Institutes of Health (NIH)	GM144982	Eric Greene
HHS | National Institutes of Health (NIH)	GM145238	James S Fraser
HHS | National Institutes of Health (NIH)	GM149542	Justin M Kollman

Author ORCID iDs

Eric Greene: https://orcid.org/0000-0003-1717-0914
Markus Tecson CB Tecson: https://orcid.org/0009-0004-6594-5467
Massimiliano Bonomi: https://orcid.org/0000-0002-7321-0004
Justin M Kollman: https://orcid.org/0000-0002-0350-5827
James S Fraser: https://orcid.org/0000-0002-5080-2859

References

Abraham Mark James, Murtola Teemu, Schulz Roland, et al. (2015) GROMACS: High Performance Molecular Simulations through Multi-Level Parallelism from Laptops to Supercomputers. *SoftwareX* **1-2**:19-25 https://doi.org/10.1016/j.softx.2015.06.001

Albe KR, Butler MH, Wright BE (1990) Cellular Concentrations of Enzymes and Their Substrates. *Journal of Theoretical Biology* **143**:163-195 https://doi.org/10.1016/s0022-5193(05)80266-8 | PubMed

Arad G, Freikopf A, Kulka RG (1976) Glutamine-Stimulated Modification and Degradation of Glutamine Synthetase in Hepatoma Tissue Culture Cells. *Cell* **8**:95-101 https://doi.org/10.1016/0092-8674(76)90190-2 | PubMed

Atkinson DE (1965) Biological Feedback Control at the Molecular Level. *Science (New York, N.Y.)* **150**:851-857 https://doi.org/10.1126/science.150.3698.851 | PubMed

Berendsen HJC, Postma JPM, van Gunsteren WF, DiNola A, Haak JR (1984) Molecular Dynamics with Coupling to an External Bath. *The Journal of Chemical Physics* **81**:3684-3690 https://doi.org/10.1063/1.448118

Bussi Giovanni, Donadio Davide, Parrinello Michele (2007) Canonical Sampling through Velocity Rescaling. *The Journal of Chemical Physics* **126**:014101 https://doi.org/10.1063/1.2408420 | PubMed

de Carvalho Fernandes Gabriela, Turchetto-Zolet Andreia Carina, Pereira Passaglia Luciane Maria (2022) Glutamine Synthetase Evolutionary History Revisited: Tracing Back beyond the Last Universal Common Ancestor. *Evolution; International Journal of Organic Evolution* **76**:605-622 https://doi.org/10.1111/evo.14434

Castegna Alessandra, Menga Alessio (2018) Glutamine Synthetase: Localization Dictates Outcome. *Genes* **9**:108 https://doi.org/10.3390/genes9020108 | PubMed

Cui Qiang, Karplus Martin (2008) Allostery and Cooperativity Revisited. *Protein Science: A Publication of the Protein Society* **17**:1295-1307 https://doi.org/10.1110/ps.03259908 | PubMed

Dasarathy Srinivasan, Mookerjee Rajeshwar P, Rackayova Veronika, et al. (2017) Ammonia Toxicity: From Head to Toe?. *Metabolic Brain Disease* **32**:529-538 https://doi.org/10.1007/s11011-016-9938-3 | PubMed

Eisenberg D, Gill HS, Pfluegl GM, Rotstein SH (2000) Structure-Function Relationships of Glutamine Synthetases. *Biochimica et Biophysica Acta* **1477**:122-145 https://doi.org/10.1016/s0167-4838(99)00270-8 | PubMed

Engel Stacia R, Aleksander Suzi, Nash Robert S, et al. (2025) Saccharomyces Genome Database: Advances in Genome Annotation, Expanded Biochemical Pathways, and Other Key Enhancements. *Genetics* **229**:iyae185 https://doi.org/10.1093/genetics/iyae185 | PubMed

Essmann Ulrich, Perera Lalith, Berkowitz Max L, Darden Tom, Lee Hsing, Pedersen Lee G (1995) A Smooth Particle Mesh Ewald Method. *The Journal of Chemical Physics* **103**:8577-8593 https://doi.org/10.1063/1.470117

Frieg Benedikt, Görg Boris, Homeyer Nadine, Keitel Verena, Häussinger Dieter, Gohlke Holger (2016) Molecular Mechanisms of Glutamine Synthetase Mutations That Lead to Clinically Relevant Pathologies. *PLoS Computational Biology* **12**:e1004693 https://doi.org/10.1371/journal.pcbi.1004693 | PubMed

Fung Tak Shun, Ryu Keun Woo, Thompson Craig B (2025) Arginine: At the Crossroads of Nitrogen Metabolism. *The EMBO Journal* **44**:1275-1293 https://doi.org/10.1038/s44318-025-00379-3 | PubMed

Gerhart JC, Pardee AB (1962) The Enzymology of Control by Feedback Inhibition. *The Journal of Biological Chemistry* **237**:891-896 https://doi.org/10.1016/s0021-9258(18)60389-8 | PubMed

Guerrero Fernando, Ciragan Annika, Iwaï Hideo (2015) Tandem SUMO Fusion Vectors for Improving Soluble Protein Expression and Purification. *Protein Expression and Purification* **116**:42-49 https://doi.org/10.1016/j.pep.2015.08.019 | PubMed

He Yong-Xing, Gui Long, Liu Yin-Zi, et al. (2009) Crystal Structure of Saccharomyces Cerevisiae Glutamine Synthetase Gln1 Suggests a Nanotube-like Supramolecular Assembly. *Proteins* **76**:249-254 https://doi.org/10.1002/prot.22403 | PubMed

Hoff Samuel E, Emil Thomasen F, Lindorff-Larsen Kresten, Bonomi Massimiliano (2024) Accurate Model and Ensemble Refinement Using Cryo-Electron Microscopy Maps and Bayesian Inference. *PLoS Computational Biology* **20**:e1012180 https://doi.org/10.1371/journal.pcbi.1012180 | PubMed

Huang Pei-Chi, Chen Shao-Kang, Chiang Wei-Hung, Ho Meng-Ru, Wu Kuen-Phon (2022) Structural Basis for the Helical Filament Formation of Escherichia Coli Glutamine Synthetase. *Protein Science: A Publication of the Protein Society* **31**:e4304 https://doi.org/10.1002/pro.4304 | PubMed

Hvorecny Kelli L, Hargett Kenzee, Quispe Joel D, Kollman Justin M (2023) Human PRPS1 Filaments Stabilize Allosteric Sites to Regulate Activity. *Nature Structural & Molecular Biology* **30**:391-402 https://doi.org/10.1038/s41594-023-00921-z | PubMed

Hvorecny Kelli L, Kollman Justin M (2023) Greater than the Sum of Parts: Mechanisms of Metabolic Regulation by Enzyme Filaments. *Current Opinion in Structural Biology* **79**:102530 https://doi.org/10.1016/j.sbi.2023.102530 | PubMed

Issoglio Federico M, Campolo Nicolas, Zeida Ari, et al. (2016) Exploring the Catalytic Mechanism of Human Glutamine Synthetase by Computer Simulations. *Biochemistry* **55**:5907-5916 https://doi.org/10.1021/acs.biochem.6b00822 | PubMed

Johnson Kenneth A (2019) New Standards for Collecting and Fitting Steady State Kinetic Data. *Beilstein Journal of Organic Chemistry* **15**:16-29 https://doi.org/10.3762/bjoc.15.2 | PubMed

Johnson Matthew C, Kollman Justin M (2020) Cryo-EM Structures Demonstrate Human IMPDH2 Filament Assembly Tunes Allosteric Regulation. *eLife* **9**:January https://doi.org/10.7554/eLife.53243 | PubMed

Jo Sunhwan, Kim Taehoon, Iyer Vidyashankara G, Im Wonpil (2008) CHARMM-GUI: A Web-Based Graphical User Interface for CHARMM. *Journal of Computational Chemistry* **29**:1859-1865 https://doi.org/10.1002/jcc.20945 | PubMed

Krajewski Wojciech W, Collins Ruairi, Holmberg-Schiavone Lovisa, Alwyn Jones T, Karlberg Tobias, Mowbray Sherry L (2008) Crystal Structures of Mammalian Glutamine Synthetases Illustrate Substrate-Induced Conformational Changes and Provide Opportunities for Drug and Herbicide Design. *Journal of Molecular Biology* **375**:217-228 https://doi.org/10.1016/j.jmb.2007.10.029 | PubMed

Lynch Eric M, Kollman Justin M, Webb Bradley A (2020) Filament Formation by Metabolic Enzymes-A New Twist on Regulation. *Current Opinion in Cell Biology* **66**:28-33 https://doi.org/10.1016/j.ceb.2020.04.006 | PubMed

MacKerell AD, Bashford D, Bellott M, et al. (1998) All-Atom Empirical Potential for Molecular Modeling and Dynamics Studies of Proteins. *The Journal of Physical Chemistry. B* **102**:3586-3616 https://doi.org/10.1021/jp973084f | PubMed

Mathy Christopher JP, Kortemme Tanja (2023) Emerging Maps of Allosteric Regulation in Cellular Networks. *Current Opinion in Structural Biology* **80**:102602 https://doi.org/10.1016/j.sbi.2023.102602 | PubMed

Matreyek Kenneth A, Stephany Jason J, Chiasson Melissa A, Hasle Nicholas, Fowler Douglas M (2020) An Improved Platform for Functional Assessment of Large Protein Libraries in Mammalian Cells. *Nucleic Acids Research* **48**:e1 https://doi.org/10.1093/nar/gkz910 | PubMed

Matreyek Kenneth A, Stephany Jason J, Fowler Douglas M (2017) A Platform for Functional Assessment of Large Variant Libraries in Mammalian Cells. *Nucleic Acids Research* **45**:e102 https://doi.org/10.1093/nar/gkx183 | PubMed

Moreira Cátia, Ramos Maria J, Fernandes Pedro A (2017) Clarifying the Catalytic Mechanism of Human Glutamine Synthetase: A QM/MM Study. *The Journal of Physical Chemistry. B* **121**:6313-6320 https://doi.org/10.1021/acs.jpcb.7b02543 | PubMed

Noree Chalongrat, Begovich Kyle, Samilo Dane, Broyer Risa, Monfort Elena, Wilhelm James E (2019) A Quantitative Screen for Metabolic Enzyme Structures Reveals Patterns of Assembly across the Yeast Metabolic Network. *Molecular Biology of the Cell* **30**:2721-2736 https://doi.org/10.1091/mbc.e19-04-0224 | PubMed

Owji Aaron P, Yu Kuai, Kittredge Alec, Wang Jiali, Zhang Yu, Yang Tingting (2022) Bestrophin-2 and Glutamine Synthetase Form a Complex for Glutamate Release. *Nature* **611**:180-187 https://doi.org/10.1038/s41586-022-05373-x | PubMed

Park Chad K, Horton Nancy C (2019) Structures, Functions, and Mechanisms of Filament Forming Enzymes: A Renaissance of Enzyme Filamentation. *Biophysical Reviews* **11**:927-994 https://doi.org/10.1007/s12551-019-00602-6 | PubMed

Petrovska Ivana, Nüske Elisabeth, Munder Matthias C, et al. (2014) Filament Formation by Metabolic Enzymes Is a Specific Adaptation to an Advanced State of Cellular Starvation. *eLife* **3**:e02409 https://doi.org/10.7554/eLife.02409

consortium PLUMED (2019) Promoting Transparency and Reproducibility in Enhanced Molecular Simulations. *Nature Methods* **16**:670-673 https://doi.org/10.1038/s41592-019-0506-8 | PubMed

Rajendra Yashas, Kiseljak Divor, Baldi Lucia, Hacker David L, Wurm Florian M (2011) Influence of Glutamine on Transient and Stable Recombinant Protein Production in CHO and HEK-293 Cells. *BMC Proceedings* **5**:P35 https://doi.org/10.1186/1753-6561-5-s8-p35 | PubMed

Rigual María Del Mar, Angulo-Aguado Mariana, Zagorac Sladjana, et al. (2025) Macrophages Harness Hepatocyte Glutamate to Boost Liver Regeneration. *Nature* **641**:1005-1016 https://doi.org/10.1038/s41586-025-08778-6 | PubMed

Shapiro Bennett M, Stadtman ER (1970) [130] Glutamine Synthetase (Escherichia Coli). *Methods in Enzymology* **17**:910-922 https://doi.org/10.1016/0076-6879(71)17305-3

Spodenkiewicz Marta, Diez-Fernandez Carmen, Rüfenacht Véronique, Gemperle-Britschgi Corinne, Häberle Johannes (2016) Minireview on Glutamine Synthetase Deficiency, an Ultra-Rare Inborn Error of Amino Acid Biosynthesis. *Biology* **5**:40 https://doi.org/10.3390/biology5040040 | PubMed

Tecson Markus CB, Geluz Cyrina, Cruz Yuly, Greene Eric R (2025) Glutamine Synthetase: Diverse Regulation and Functions of an Ancient Enzyme. *Biochemistry* **64**:547-554 https://doi.org/10.1021/acs.biochem.4c00763 | PubMed

Tribello Gareth A, Bonomi Massimiliano, Branduardi Davide, Camilloni Carlo, Bussi Giovanni (2014) PLUMED 2: New Feathers for an Old Bird. *Computer Physics Communications* **185**:604-613 https://doi.org/10.1016/j.cpc.2013.09.018

Van Nguyen Thang (2021) USP15 Antagonizes CRL4CRBN-Mediated Ubiquitylation of Glutamine Synthetase and Neosubstrates. *Proceedings of the National Academy of Sciences of the United States of America* **118**:e2111391118 https://doi.org/10.1073/pnas.2111391118 | PubMed

Van Nguyen Thang, Li Jing, Lu Chin-Chun Jean, et al. (2017) p97/VCP Promotes Degradation of CRBN Substrate Glutamine Synthetase and Neosubstrates. *Proceedings of the National Academy of Sciences of the United States of America* **114**:3565-3571 https://doi.org/10.1073/pnas.1700949114 | PubMed

Van Nguyen T, Eugene Lee J, Sweredoski Michael J, et al. (2016) Glutamine Triggers Acetylation-Dependent Degradation of Glutamine Synthetase via the Thalidomide Receptor Cereblon. *Molecular Cell* **61**:809-820 https://doi.org/10.1016/j.molcel.2016.02.032 | PubMed

Vanommeslaeghe K, Hatcher E, Acharya C, et al. (2010) CHARMM General Force Field: A Force Field for Drug-like Molecules Compatible with the CHARMM All-Atom Additive Biological Force Fields. *Journal of Computational Chemistry* **31**:671-690 https://doi.org/10.1002/jcc.21367 | PubMed

Wiśniewski Jacek R, Hein Marco Y, Cox Jürgen, Mann Matthias (2014) A 'Proteomic Ruler' for Protein Copy Number and Concentration Estimation without Spike-in Standards. *Molecular & Cellular Proteomics : MCP* **13**:3497-3506 https://doi.org/10.1074/mcp.m113.037309 | PubMed

Yu Da Young, Lee Sang Yoon, Lee Gyun Min (2018) Glutamine Synthetase Gene Knockout-Human Embryonic Kidney 293E Cells for Stable Production of Monoclonal Antibodies. *Biotechnology and Bioengineering* **115**:1367-1372 https://doi.org/10.1002/bit.26552 | PubMed

Zhao Zhenguang, Xu Wenqing, Feng Ethan Yang, et al. (2025) PCMT1 Generates the C-Terminal Cyclic Imide Degron on CRBN Substrates. *bioRxiv* https://doi.org/10.1101/2025.03.24.645050 | PubMed

Peer reviews

Reviewer #1 (Public review):

Summary:

The study is methodologically solid and introduces a compelling regulatory model. However, several mechanistic aspects and interpretations require clarification or additional experimental support to strengthen the conclusions.

Strengths:

(1) The manuscript presents a compelling structural and biochemical analysis of human glutamine synthetase, offering novel insights into product-induced filamentation.

(2) The combination of cryo-EM, mutational analysis, and molecular dynamics provides a multifaceted view of filament assembly and enzyme regulation.

(3) The contrast between human and E. coli GS filamentation mechanisms highlights a potentially unique mode of metabolic feedback in higher organisms.

Comment on revised version.

The authors have addressed all of my comments and concerns. The revisions have substantially improved the quality of the manuscript. I have no further questions or concerns.

https://doi.org/10.7554/eLife.108336.2.sa3

Reviewer #2 (Public review):

Major concern 1: The manuscript does not clearly establish a bona fide GS filament state.

The authors repeatedly refer to GS "filaments," but the data presented appear to support primarily a di-decameric assembly rather than a well-defined filamentous polymer.

A two-decamer reconstruction can define a putative inter-decamer interface, but it cannot by itself demonstrate propagation of a repeating filament geometry. To establish a bona fide filament, the authors should provide evidence for a reproducible one-dimensional assembly, such as at least three consecutive repeating units or equivalent quantitative evidence that the same inter-decamer transform propagates along an assembly axis.

In the current manuscript, many of the supporting 2D classifications appear to contain at most two adjacent GS decamers. This is particularly evident in the time-resolved cryo-EM datasets shown in Supplementary Figures 9-10, where I do not see convincing 2D classes corresponding to filaments. The same concern applies to other datasets, including Supplementary Figures 2, 6, and 11, where the apparent assemblies are primarily two-decamer particles.

Moreover, many of the selected "filament" classes show only one well-resolved GS decamer, while the neighboring decamer density is blurred. This suggests substantial variability in the relative position and/or orientation of adjacent decamers. Such heterogeneity is difficult to reconcile with a stable repeating filament geometry.

Therefore, the authors should explicitly define what they mean by "filament." If their evidence supports only a di-decameric or short oligomeric assembly, the terminology should be changed accordingly throughout the manuscript.

Symmetry concern

Given the low quality and heterogeneity of the 2D classifications for the putative "filament" classes, the use of D5 symmetry requires stronger justification. The current reconstructions primarily show the result after applying D5 symmetry to a two-decamer assembly. The

authors should show reconstructions of the same particle sets processed under C1, C5, and D5 symmetry, and explain why D5 symmetry is justified.

This is particularly important because the claimed interface density and ligand interpretation are sensitive to symmetry averaging. Without showing how the reconstruction behaves under less restrictive symmetry assumptions, it is difficult to determine whether the final D5 map reflects a true biological assembly or a symmetry-imposed interpretation.

Filament abundance and physiological relevance

Even under the authors' broad classification criteria, the filament-like population appears to be a minor species. In some datasets, especially Supplementary Figure 10, the apparent filament fraction is very low, approximately 2-10%. This raises a major concern: if GS filaments are rare even under high-concentration cryo-EM conditions, are they expected to form to a meaningful extent under physiological conditions?

The authors propose a concentration-dependent assembly mechanism. If so, the relevance of GS filamentation in the lower-concentration cellular environment becomes even less clear. The authors should quantify filament abundance as a function of GS concentration and glutamine concentration, ideally under conditions closer to physiological ranges.

K52/C53 interface mutations

The authors use K52 and C53 as filament-interface residues, but the mechanistic contribution of these residues to filament assembly remains insufficiently explained. Why should K52A or C53A disrupt filament formation? Is the effect due to loss of a specific side-chain contact, altered local electrostatics, reduced crosslinker accessibility/reactivity, local structural destabilization, or nonspecific disruption of the interface?

The manuscript states that the interface is "concentration dependent and driven primarily by electrostatic interactions," but the data presented before that statement do not clearly establish this. The authors should explicitly identify the interacting electrostatic partners and provide structural or biochemical evidence supporting this interpretation.

Functional linkage between filamentation and kinetics is weak.

The authors should establish the oligomeric state of GS under the actual assay conditions. In particular, what is the filament fraction during the Figure 2F / Supplementary Figure 15 kinetic assays? Is the change in KM ammonia quantitatively correlated with filament abundance?

This is currently unclear. The direct comparison between decamer and 2-decamer fractions does not robustly show a functional difference, and the later glutamine-addition assays are interpreted as filament-mediated without directly demonstrating the filament fraction under the same assay conditions.

In Figure 2F, WT, K52A, and C53A already show different ammonia-dependent kinetic parameters in the absence of added glutamine. K52A and C53A appear to have lower basal kcat/KM ammonia and higher KM ammonia than WT even without glutamine. The authors should explain why these interface mutants already alter basal ammonia kinetics. Without such an explanation, K52A and C53A cannot be treated as clean controls that selectively disrupt glutamine-stabilized filamentation.

Major concern 2: The interface density is not convincingly assigned to glutamine.

The second foundational issue is the assignment of the interface density to glutamine. At present, the evidence is not sufficient to support the conclusion that glutamine is the ligand at this interface.

The local density at the interface appears weak and likely has lower local resolution than the reported global resolution. The current density could represent a low-occupancy or symmetry-averaged amino-acid-like density rather than a confidently assigned glutamine molecule.

Ligand pose and hydrogen bonding.

The proposed glutamine pose also requires more rigorous validation. The authors state that glutamine forms hydrogen bonds with interface residues, including K52, C53, and E55. These hydrogen bonds should be shown explicitly in a figure, with distances listed.

The proposed interaction involving C53 appears unusual and should be justified chemically and geometrically.

Glutamate has not been excluded.

The largest problem is that the authors do not adequately consider glutamate as an alternative ligand. They compare the density with phosphate and ATP/ADP, but this is not sufficient. Glutamate is present at high concentration during turnover, and it is chemically and structurally very similar to glutamine. Given the limited local density and possible orientational averaging, distinguishing glutamine from glutamate from the current cryo-EM density alone is not justified.

The authors should report or estimate the concentrations of glutamate and glutamine at the vitrification time point used for the high-resolution turnover-filament reconstruction. If glutamate is present at a much higher concentration than glutamine, the authors must explain why the interface density should be assigned to glutamine rather than glutamate.

The authors should fit both glutamine and glutamate into the interface density using the same validation criteria and compare the results. Stronger support would come from direct structural experiments, such as cryo-EM structures of GS incubated separately with glutamate and glutamine under controlled conditions.

Unless stronger evidence is provided, the claim that "glutamine binds to the filament interface" cannot be made.

Specific comments

Interface assembly statement:

"These data suggest that the formation of the interface is concentration dependent and driven primarily by electrostatic interactions."

What specific data support "concentration dependent" at this point in the manuscript? Which residues or chemical groups are proposed to form the electrostatic interactions? The authors should provide a more explicit explanation.

Line 149-150:

"In both scenarios, any signal is likely to be averaged out and experiments with symmetry expansion and focused classification did not yield any convincing density."

Please show these analyses. Negative results are important here because they bear directly on the reliability of the interface interpretation.

"Glutamine stabilizes larger GS filaments":

What does "larger" mean? Longer filaments, more decamers per filament, or larger diameter? The authors should define this quantitatively, preferably by reporting filament-length distributions or the number of decamers per assembly.

Filament classification:

The criteria used to classify particles or 2D classes as "filament" are not sufficiently clear. The authors should provide the full 2D classification results for each time-resolved dataset, including selected and discarded classes, particle numbers, and objective selection criteria. Some selected and discarded classes appear visually similar, especially in Supplementary Figures 9-10.

R298A decamer:

The R298A mutant is presented as a turnover-decamer structure, not a filament structure. The authors should clarify whether R298A forms filament-like particles under comparable turnover conditions. If R298A does not form filaments, this should be reported and explained. If filament-like particles were present but excluded during processing, the authors should provide their abundance and justify why only the decameric form was analyzed. This point matters because R298A is used to connect E305-loop disorder with the proposed filament-associated mechanism, although R298A is a loop-stabilization mutant rather than a filament-interface mutant.

Line 231-233:

"a reaction time that should yield a high concentration of product due to the higher enzyme concentration than previous experiments"

What is the estimated product concentration at vitrification? What concentration range qualifies as "high"? The authors should provide a quantitative estimate.

Glutamine hydrogen bonds:

The proposed hydrogen bonds linking glutamine to K52, C53, and E55 should be shown explicitly with atom identities and distances.

Glutamate comparison:

What is the glutamate concentration in the same sample? Given that glutamate is chemically similar to glutamine and likely present at high concentration, why is the interface density not glutamate? The authors should compare glutamine and glutamate fitting using the same validation criteria.

Line 248-253:

The speculation that apo filaments may arise from high GS concentration or residual glutamine should be moved to the Discussion. In the Results, this reads as an ad hoc explanation rather than a result directly supported by data.

Actual assay-state oligomeric distribution:

What is the filament fraction under the actual kinetic assay conditions? Is the KM ammonia change quantitatively correlated with filament abundance?

Figure 2F:

Why do WT, K52A, and C53A differ in basal ammonia-dependent activity even without added glutamine? The authors should explain whether these mutations alter intrinsic ammonia

kinetics independent of filamentation.

Supplementary Figure 15 / Figure 2F:

Please clarify the relationship between Figure 2F and Supplementary Figure 15. The kinetic constants in Figure 2F appear to depend on global fitting of progress curves shown in Supplementary Figure 15. The authors should provide replicate-level raw progress curves, between-replicate variability, fitting residuals, and individual fitted parameters.

Supplementary Figure 19:

Supplementary Figure 19 should be presented consistently with Supplementary Figure 18, including the corresponding 2D classification results.

In summary, although the revised manuscript improves the presentation of cryo-EM map processing, the two foundational claims remain unresolved. The current data establish, at most, a di-decameric or filament-like GS assembly, but not a rigorously defined filamentous polymer. In addition, the interface density is not convincingly assigned to glutamine, particularly because glutamate has not been excluded as the most relevant alternative ligand. Since the proposed negative-feedback mechanism depends directly on these two points, the current evidence does not support the strength of the title, abstract, or mechanistic conclusions.

https://doi.org/10.7554/eLife.108336.2.sa2

Reviewer #3 (Public review):

In this manuscript, the authors propose a product-dependent negative-feedback mechanism of human glutamine synthetase, whereby the product glutamine facilitates filament formation, leading to reduced catalytic specificity for ammonia. Using time-resolved cryo-EM, the authors demonstrate filament formation under product-rich conditions. Multiple high-quality structures, including decameric and di-decameric assemblies, were resolved under different biochemical states and combined with MD simulations, revealing that the conformational space of the active site loop is critical for the GS catalysis. The study also includes extensive steady-state kinetic assays, supporting the view that glutamine regulates GS assembly and its catalytic activity. Overall, this is a detailed and comprehensive study. However, I would advise that a few points be addressed and clarified.

Comments on revised version.

The revision addresses several reviewer concerns: the authors add sharpened maps, ligand-density panels, symmetry expansion/focused classification, biochemical blank/substrate/TCEP controls, and E305-loop focused classification. The E305-loop part is stronger now: turnover decamer recovers partial E-flap density in few classes, while turnover filament does not.

My only remaining comment is that - as also the authors agree on the need to integrate density with biochemical data and that local resolution/averaging complicates modeling - I would advise softening the claim regarding glutamine from "glutamine binds" to "density consistent with glutamine/product-associated density". In general, it would be best to avoid overstating atomic certainty at the filament interface and the safest framing is the observed interface density is compatible with glutamine but not independently conclusive.

https://doi.org/10.7554/eLife.108336.2.sa1

Author response:

The following is the authors' response to the original reviews.

Public Reviews:

Reviewer #1 (Public review):

Summary:

The study is methodologically solid and introduces a compelling regulatory model. However, several mechanistic aspects and interpretations require clarification or additional experimental support to strengthen the conclusions.

Strengths:

(1) The manuscript presents a compelling structural and biochemical analysis of human glutamine synthetase, offering novel insights into product-induced filamentation.

(2) The combination of cryo-EM, mutational analysis, and molecular dynamics provides a multifaceted view of filament assembly and enzyme regulation.

(3) The contrast between human and E. coli GS filamentation mechanisms highlights a potentially unique mode of metabolic feedback in higher organisms.

Weaknesses:

(1) The mechanism underlying spontaneous di-decamer formation in the absence of glutamine is insufficiently explored and lacks quantitative biophysical validation.

(2) Claims of decamer-only behavior in mutants rely solely on negative-stain EM and are not supported by orthogonal solution-based methods.

We thank the reviewer for the summary and noting of the strengths. We agree that the evolutionary divergence of metabolic feedback in GS homologs is a fruitful avenue for future studies. With regard to the weaknesses, the di-decamer in the absence of glutamine only forms under high (higher than physiological) concentrations of enzyme. Our primary evidence for the mutant behavior was the lack of crosslinking (Figure 1E), with supplementary support from the negative stain. In the revised version we will soften the language to say “reduced” rather than “did not support” filament formation.

Reviewer #2 (Public review):

The authors set out to resolve the high-resolution structure of a glutamine synthetase (GS) decamer using cryo-EM, investigate glutamine binding at the decamer interface, and validate structural observations through biochemical assays of ATP hydrolysis linked to enzyme activity. Their work sits at the intersection of structural and functional biology, aiming to bridge atomic-level details with biological mechanisms - a goal with clear relevance to researchers studying enzyme catalysis and metabolic regulation.

Strengths and weaknesses of methods and results:

A key strength of the study lies in its use of cryo-EM, a technique well-suited for resolving large, dynamic macromolecular complexes like the GS decamer. The reported resolutions (down to 2.15 Å) initially suggest the potential for detailed structural insights, such as side-chain interactions and ligand density. However, several methodological limitations significantly undermine the reliability of the results:

(1) Cryo-EM data processing: The absence of critical details about B-factor sharpening - a standard step to enhance map interpretability - is a major concern. For high-resolution maps (<3 Å), sharpening is typically applied to resolve side-chain features, yet the submitted maps (e.g., those in Figures 1D, 2D, and supplementary figures) appear

unprocessed, with density quality inconsistent with the claimed resolutions. This makes it difficult to evaluate whether observed features (e.g., glutamine binding) are genuine or artifacts of unsharpened data.

(2) Modeling and density consistency: The structural models, particularly for glutamine binding at the decamer interface, do not align with the reported resolution. The maps shown in Figure 2D and Supplementary Figure S7 lack sufficient density to confidently place glutamine or even surrounding residues, conflicting with claims of 2.15 Å resolution. Additionally, fitting a non-symmetric ligand (glutamine) into a symmetry-refined map requires justification, as symmetry constraints may distort ligand placement.

(3) Biochemical assay controls: While the enzyme activity assays aim to link structure to function, they lack essential controls (e.g., blank reactions without GS or substrates, substrate omission tests) to confirm that ATP hydrolysis is GS-dependent. The use of TCEP, a reducing agent, is also not paired with experiments to rule out unintended effects on the PK/LDH system, further limiting confidence in activity measurements.

Achievement of aims and support for conclusions:

The study falls short of convincingly achieving its goals. The claimed high-resolution structural details (e.g., side-chain densities, ligand binding) are not supported by the provided maps, which lack sharpening and show inconsistencies in density quality. Similarly, the biochemical data do not robustly validate the structural claims due to missing controls. As a result, the evidence is insufficient to confirm glutamine binding at the decamer interface or the functional relevance of the observed structural features.

Likely impact and utility:

If these methodological gaps are addressed, the work could make a meaningful contribution to the field. A well-resolved GS decamer structure would advance understanding of enzyme assembly and ligand recognition, while validated biochemical assays would strengthen the link between structure and function. Improved data processing and clearer reporting of validation steps would also make the structural data more reliable for the community, providing a resource for future studies on GS or related enzymes.

We disagree with the reviewer's overall assessment.

With regard to sharpening and resolution: we examined sharpened maps and in a revised version will present additional supplementary figures showing these maps side by side. We note that the resolutions reported are global and that the most interesting features are, of course, in the periphery and subject to conformational and compositional heterogeneity. We will include supplementary figures of core side chain densities that are more like what are expected by the reviewer in the revision. With regard to modeling: the apo filament and turnover filament datasets were handled nearly identically. The additional density is therefore likely not artefactual to the symmetry operator - however, the lower resolution in this region noted by the reviewer is worthy of further exploration. The maps are public and we think this is the most plausible interpretation of the density, which we based primarily on the biochemical data and will include more speculation in the version.

With regard to the biochemical controls: we point the reviewer to Figure S1, which shows that omission of ammonia or glutamate in the wild-type (tagless) system removes any coupling of the reactions. We will perform the additional controls to publication quality in the revised version along with the TCEP control. We note that the reducing agent is present across all experiments, ruling out an effect on any specific result. The inclusion of TCEP is

also very standard in other published uses of the Coupled ATPase assay (e.g. PMID: 31778111 and PMID: 32483380 by our first author)

> *Additional context:*
>
> *Cryo-EM has transformed structural biology by enabling high-resolution analysis of large complexes, but its success hinges on rigorous data processing and validation steps that are critical to ensuring reproducibility. The challenges highlighted here are not unique to this study; they reflect broader issues in the field where incomplete reporting of methods can obscure the reliability of results. By addressing these points, the authors would not only strengthen their current work but also set a positive example for transparent and rigorous structural biology research.*

All the data is public and the reviewer or anyone is free to reinterpret the maps and models - and we encourage that rather than just an interpretation of our static figures. In addition, we will upload the raw micrograph data for the apo filament and turnover filament datasets to EMPIAR prior to submitting the revision.

> ***Reviewer #3 (Public review):***
>
> *In this manuscript, the authors propose a product-dependent negative-feedback mechanism of human glutamine synthetase, whereby the product glutamine facilitates filament formation, leading to reduced catalytic specificity for ammonia. Using time-resolved cryo-EM, the authors demonstrate filament formation under product-rich conditions. Multiple high-quality structures, including decameric and di-decameric assemblies, were resolved under different biochemical states and combined with MD simulations, revealing that the conformational space of the active site loop is critical for the GS catalysis. The study also includes extensive steady-state kinetic assays, supporting the view that glutamine regulates GS assembly and its catalytic activity. Overall, this is a detailed and comprehensive study. However, I would advise that a few points be addressed and clarified.*
>
> *(1) In Figure 2D and Supplementary Figure 7, the extra density observed between the two decamers does not appear to have the defining features of a glutamine. A less defined density may be expected given the nature of the complex, but even though mutagenesis assays were performed to support this assignment, none of these results constitutes direct and conclusive evidence for glutamine binding at this site. I would thus suggest showing the density maps at multiple contour thresholds to allow readers to also better evaluate the various small molecules under turnover conditions that cannot be well fitted based on this density map, helping to provide a more balanced interpretation of the results.*
>
> *(2) On the same point regarding the density for the enzyme under turnover conditions, more details should be provided about the symmetry expansion and classification performed, and also show the approximate ratio of reconstructions that include this density. Did you try symmetry expansion followed by focused classification, especially on the interface region?*
>
> *(3) The interface between the two decamers of the model needs to be double-checked and reassigned, especially for the residues surrounding the fitted glutamine. For example, the side chain of the Lys residue shown in the attached figure is most likely modeled incorrectly.*

We thank the reviewer for the feedback. As noted above, we will include supplemental figures that show maps at multiple thresholds and sharpening schemes. We noted in the manuscript and above that our interpretation here is based on integrating biochemical evidence alongside the density and will make that even more clear in the revised manuscript.

The filaments +/- the putative glutamine density were processed nearly identically, but we will attempt various schemes of focused classification/symmetry expansion in the revision as well. However, we point out that there is extensive averaging there that makes modeling a bit trickier than expected given the global resolution.

> ***Recommendations for the authors:***
>
> ***Reviewer #1 (Recommendations for the authors):***
>
> *Major Comments*
>
> *(1) Limitation to Di-decamer Formation:*
>
> *Could the authors clarify why hGS, when visualized by cryo-EM, predominantly forms di-decamers rather than extended filaments? Since glutamine bridges the two decameric rings, one would expect this to promote further polymerization. It remains unclear why longer filaments are not observed under the conditions used. Moreover, data in Figure 1B-1D are not mixed with Gln, and the mechanism of the apo-form filament formation is not clearly discussed. If K52 and C53 are in charge of filamentation, it is supposed to form a long filament, not a stack of 2 decamers. The kinetics of wild type and mutations, including K52A and C53A, are different. This confused me as K52 and C53 don't participate in the reactions of glutamine synthesis. Does data reduce catalytic efficiency with K52A or C53A mutation suggest that di-decameric GS exhibits a greater catalytic turnover rate than the pure decameric GS?*

We thank the reviewer for pointing this out and it was indeed filament length that was a point of curiosity during the study. Prior to preprint, we repeated the freezing conditions under identical turnover conditions and with high protein concentration as reported and indeed found much longer filaments - pointing to the capacity of the system to form larger complexes. However, we only captured a couple of 'screening' images and did not collect a full second dataset. Therefore, we hypothesize that filament length may be stochastic based on the subtle differences of individual grid vitrification based on the assumption that decamers within a filament can freely and quickly exchange. However, as shown in the time-resolved cryoEM experiment, the fraction of particles that are characterized as participating in a filament form (length-agnostic metric), does not appear to be subject to individual grid vitrification conditions but rather by experimental conditions (concentration of reaction-derived glutamine).

The filament formation in apo state was not further explored because the concentrations required to achieve filament formation in this case were supraphysiological.

We have edited the discussion to emphasize this point more clearly:

"While the enzyme concentrations to achieve robust filamentation in the absence of glutamine are much higher than observed in cells, the protein concentrations used in our time-resolved cryoEM experiments where filamentation is correlated with accumulation of glutamine are within the range of intracellular GS concentrations in S. cerevisiae (Engel et al. 2025) and human cell lines (Wiśniewski et al. 2014)."

Regarding the ability of apo-GS to form filaments - we identified that these residues were important based on their structural location at the decamer: decamer interface (Figure 1D; away from the active site as pointed out) and because their individual mutation to alanine attenuated the ability to form higher order filaments (Figure 1E). Therefore, these mutants were crucial controls in the steady-state kinetic experiments reported (Figure 2E). Here, we used exogenous glutamine to seed/stabilize filaments because we identified glutamine as serving this function and, crucially, because we did not observe glutamine occupancy in the active site under turnover conditions (which would suggest an orthosteric feedback

inhibition mechanism; Supplementary Figure 10). Under these conditions, the wild-type, filament-competent protein displayed a ~3-fold $K_{M,\ ammonia}$ increase with glutamine addition compared to no glutamine, which when considered in the context of the greater E-305 flap conformational heterogeneity speaks to a model of allosteric feedback inhibition. Importantly, K52A and C53A show no difference in $K_{M,\ ammonia}$ between the glutamine and no glutamine condition, suggesting that attenuation of filament formation at this interface via mutation, eliminates the kinetic deficit. Therefore, K52A and C53A are not product-inhibited in the same manner as wild-type GS.

We have clarified the discussion to emphasize this result:

"Importantly, point mutations of the interfacial residues do not show a $K_{M,\ ammonia}$ defect in the presence of glutamine, indicative of the importance of the filament form for product feedback."

> *(2) Origin of Di-decamer Formation in the Absence of Glutamine:*
>
> *While the manuscript demonstrates glutamine-stabilized filamentation, the spontaneous formation of di-decamers under apo conditions is not mechanistically explained. The observation of 10-mer, 20-mer, and 40-mer species in Figure 1B should be validated against molecular weight standards or through SEC-MALS. The inference of higher-order oligomers based solely on migration is insufficient. Additional characterization (e.g., SEC-MALS, AUC, or mass photometry) would clarify whether these assemblies are biologically relevant or incidental.*

We thank the reviewer for pointing out the low precision of preparatory size exclusion chromatography assignments of GS molecular weight filament depicted in Figure 1. We have included calibration standards and assignment in Supplementary Figure 1 and updated Figure 1 to include the ambiguity of these assignments in panel B. It is important to note that GS has historically been underestimated in size via these methods and was originally assigned as an octamer for which there was previous consensus (PMID: 10708854). The low concentration requirements of mass photometry preclude its use for this purpose and we are not in a position to do SEC-MALS or AUC for this. Hopefully, the negative stain, crosslinking, and cryo-EM results are sufficient to indicate that we have correlated signals with the correct species!

> *(3) Validation of Interface Mutants as Decamer-only Species:*
>
> *K52A and C53A mutants are used to disrupt di-decamer formation and are shown by negative-stain EM to exist as decamers. While supportive, this is qualitative. The inclusion of quantitative biophysical data (e.g., SEC-MALS or mass photometry) would more convincingly demonstrate that these mutants do not transiently assemble into higher-order oligomers. Furthermore, molecular measurements describing the spatial relationship of interface residues - such as the distance between K52 and E55 or between C53 residues of opposing decamers - would aid interpretation. The use of the term "adjacent" (line 530) is vague and should be made more precise.*

We thank the reviewer for the thoughtful comments. Beyond negative-stain EM we also performed a biochemical validation of the filament interface through bi-functional crosslinking based on the premise that the new filament interface, as defined by the apo-filament structure, presented new/unique pairs of nucleophilic amino acid R-groups in close proximity. We used Bis-sulfosuccinimidyl glutarate (BSG) or bis-maleimoethane (BMOE) to covalently link adjacent primary amines and sulfhydryls respectively (Figure 1E). This experiment defines two key principles of GS filament formation in the absence of glutamine:

(1) It is concentration dependent. In the wild-type case there is a protein-dependent increase on crosslinking efficiency for both crosslinkers.

(2) It is dependent on C53 and K52. Mutation of C53 or K52 significantly attenuated crosslinking efficiency.

To make sure that these results are more prominent, we have now included a table of these intersubunit distances between epsilon amine groups of lysines and gamma sulfhydroxyl of cysteines groups based on the apo-filament structure and labeled this as either participating in the filament interface or not. Furthermore, in line with multiple reviewers comments, we have updated Figure 1D to include a sharpened representation of the map that shows strong side chain density for the amino acid side chains to further support these reported side chain distance measurements.

We thank the reviewer for pointing out the low precision of the SEC chromatogram interpretation of Figure 1B and the figure has been amended to show filaments of variable length, instead of defined length. We also included a calibration curve to Supplemental Figure 1B and estimated molecular weights. While these estimates of size are lower than ground truth it is important to note that GS has historically displayed smaller than predicted molecular weights via size exclusion chromatography and analytical ultracentrifugation where initial characterization papers defined the oligomeric state as an octamer rather than decamer (PMID: 10708854). These studies and the present indicate potential adherence to resin and/or other factors about the shape of GS that lead to longer retention. Lastly, these SEC procedures were performed as a preparative step rather than for analytical purposes, so resolution was not the ultimate goal.

> *(4) Terminology: "Scarless" hGS:*
>
> *The term "scarless human glutamine synthetase" is unconventional and potentially confusing. If it refers to the wild-type sequence lacking N- or C-terminal tags or mutations, I recommend using the term "native hGS" for clarity.*

We usually reserve “native” for proteins isolated from the original species and not recombinantly expressed (as here). So we will leave the term scarless in the document.

> *(5) Helical Parameters of Filament Assembly:*
>
> *The manuscript states a ~26{degree sign} rotation (clockwise or counterclockwise?) between decamers in the filament, yet does not describe how this value was derived. Given that hGS filaments form helices, this parameter could be assessed via helical reconstruction. Is it possible the actual helical twist is ~30{degree sign}, implying 12 stacked decamers per full turn? Please elaborate on how the rotational angle was determined.*

Rotation was determined through inspection of the apo-filament cryoEM map in ChimeraX where an outline of a pentamer from one decameric unit was rotated with respect to the outline of a pentamer across the filament interface and the rotation was measured. Helical reconstruction was not pursued in this work owing to the typically short filaments observed in micrographs and the relative ease by which a 20-mer species could be selected via traditional 2D and 3D classification/reconstruction methods.

We have added to the methods the following to better illustrate this measurement:

“Decamer: Decamer rotation across the filament interface was determined through inspection of the apo-filament cryoEM map in ChimeraX where an outline of a pentamer from one decameric unit was rotated with respect to the outline of a pentamer across the filament interface and the rotation was depicted in Figure 1D.”

> *(6) Time-Resolved Cryo-EM and Filament Growth:*

> *The use of time-resolved cryo-EM is innovative; however, the accessible timescales are relatively short. I suggest complementing this approach with techniques such as dynamic light scattering (DLS) or mass photometry, which allow extended real-time monitoring of filament assembly over longer durations (e.g., hours). These methods can also provide higher temporal resolution and particle size distributions.*

We thank the reviewer for this suggestion and agree that understanding the kinetics of filament formation is critical. While DLS and mass photometry are excellent for monitoring assembly over hours, our data indicates that GS filament formation occurs on a much faster timescale.

As shown in Figure 2C, when we added ATP and Glutamine directly to GS and vitrified the sample after only 5 minutes, the majority of particles had already formed filaments, indicating that the interaction had reached saturation. This contrasts with our time-resolved experiment, where the kinetics of filament formation were likely rate-limited by the enzymatic generation of glutamine rather than the assembly process itself.

Consequently, we anticipate that filament assembly occurs on the order of seconds or less—a timescale we interpret as a necessary prerequisite for a rapid and effective cellular feedback mechanism. Therefore, we believe the current cryo-EM data accurately captures the biologically relevant window of assembly.

> *(7) Cryo-EM Symmetry Imposition and Loop Flexibility:*
>
> *The use of D5 symmetry in cryo-EM reconstructions may obscure conformational heterogeneity in flexible elements, such as the E305 loop. Since the authors used MD simulations to characterize loop dynamics, it would strengthen the study to also perform symmetry expansion followed by non-uniform refinement and alignment-free 3D classification of individual subunits. This could provide experimental validation of the proposed conformational variability.*

We agree with the reviewer that symmetry enforcement can mask conformational heterogeneity, particularly for flexible elements like the E305 loop (the E-flap). To address this, we followed the reviewer's suggestion and performed symmetry expansion on both the turnover decamer and filament consensus maps. This was followed by focused, alignment-free 3D classification on the asymmetric unit containing the E-flap.

Our analysis revealed a clear distinction: while 4 out of 12 turnover decamer classes showed partial density for the E-flap (class 3, 7, 8, and 12)—consistent with the flexibility observed in our MD simulations—none of the turnover filament classes demonstrated similar density. To ensure a direct comparison, we utilized a C5-expanded turnover decamer map to maintain an identical asymmetric unit to the D5-expanded turnover filament map. We note here that the turnover decamer consensus volume is different from the deposited map for which no symmetry was applied.

Despite the different initial symmetries (D5 for filaments vs. C5 for decamers), we utilized a C5-expanded decamer map to maintain an identical asymmetric unit. For transparency, we have uploaded this C5-refined consensus map and all resulting 3D classification maps to Zenodo. We agree that the text is now strengthened given this result and we have added the following to the main text:

"The differential loop density between turnover-decamer and turnover-filament species was further supported by 3D classification of symmetry-expanded particles, which recovered partial E305-loop density in 4/12 turnover-decamer classes (C5; Supplemental Figure 18) compared to 0/12 classes for the turnover-filament (D5; Supplemental Figure 19)."

> *(8) Crosslinking Gel Analysis (Figure 1E):*
>
> *The SDS-PAGE gels shown in Figure 1E have molecular weight ladders cropped. For proper interpretation, please include full ladders with size markers and labels. In addition, clarify whether the crosslinked samples were denatured in reducing buffer. Crosslinking efficiency and specificity using BMOE or BSG require verification under reducing conditions (e.g., DTT, β-mercaptoethanol, or TCEP) to confirm covalent linkage between decamers.*

We have added in Figure 1E molecular weight markers estimates to aid in gel interpretation and have included the uncropped gels in Supplementary Figure 1D that contain the full MW ladder. The methods were clarified to indicate that reducing reagent was used in both the crosslinking reaction and all SDS-PAGE samples.

"Protein samples were diluted to concentrations noted in base buffer (60 mM HEPES pH 7.6, 50 mM NaCl, 50 mM KCl, 10 mM $MgCl_2$, 0.1 mM TCEP) and, reacted with crosslinker to a final concentration of 0.5 mM for 10 mins at room temperature followed by quench in 5X SDS-PAGE sample buffer (225 mM Tris pH 6.8, 50% glycerol, 0.05 % SDS, 0.2 mg/mL bromophenol blue, 1M DTT) supplemented with 100 mM of either NH_4Cl (to quench BSG reactions only) or DTT (to quench BMOE). Protein concentrations were normalized after quench prior to SDS-PAGE analysis."

> *(9) Missing Reference for NADH-Coupled Assay:*
>
> *Line 678-679 refers to an NADH-coupled assay described "previously" without citing a source. Please provide a proper reference to ensure reproducibility.*

The original paper describing the implementation of a coupled-assay to measure ADP production from glutamine synthetase was written by Bennett Shapiro and Eric Stadtman in 1970 and has been included. We will note that the conditions of this assay have been much improved since this time with better buffers, commercially available reagents of combined lactate dehydrogenase and pyruvate kinase, and modern plate readers. We added the following reference:

"Shapiro, B.M. and Stadtman, E.R., 1970. [130] Glutamine synthetase (Escherichia coli). In Methods in enzymology (Vol. 17, pp. 910-922). Academic Press."

> *(10) Unclear Description of the NADH Assay:*
>
> *The stability of NADH is influenced by pH and light exposure. Please specify the pH range used in the assay and whether precautions (e.g., light shielding) were taken. NADH autoxidation at high pH or degradation at low pH could impact assay reliability and should be addressed in the Methods section.*

For clarity and transparency the following text was added to the Methods section.

"Stocks of ATP, NADH, and phosphoenolpyruvate were made in base buffer (60 mM HEPES pH 7.6, 50 mM NaCl, 50 mM KCl, 10 mM $MgCl_2$, 0.5 mM TCEP) and the pH was adjusted until it reached 7.5 on ice prior to aliquoting, flash freezing, and storage at -80°C in the dark. NADH was only exposed to light upon thawing and assay set-up and no appreciable change in absorbance of control experiments were noted."

> *(11) Ligand Density in Figure 2 and Supplementary Figure 7:*
>
> *The density attributed to glutamine, ADP, and phosphate appears broader than expected. Please include cross-correlation (CC) values, estimated occupancies, and Q-factors for ligand fitting. Varying the contour level to assess density consistency would*

> *clarify whether the observed volume represents multiple conformations, partial occupancy, or overfitting. A similar concern applies to the cysteine sidechain density.*

We have updated Supplemental Figures to include:

(1) Globally refined map in comparison to locally refined map where both are sharpened per previous feedback.

(2) Ligand placement now also include Q-scores and CC values

We did not include multiple contour levels because these are included in the resolution representative Supplemental Figure and because alternative contours do not influence Q-scores. From this analysis it is apparent that phosphate and ADP are both worse fits to the density.

Moreover, we have now included Supplementary Table 2 that includes all ligand validation statistics for the reader to evaluate the range of B-factor, CC values, and Q-scores for all ligands in all models.

> *(12) Missing Ligand B-factors in Supplementary Table 1:*
>
> *The ligand refinement statistics in Supplementary Table 1 are incomplete. Please include B-factors and occupancy values for all ligands.*

We have updated the PDB depositions to include B-factors in .cif files that are now available. We have also included Supplementary Table 2 in the manuscript detailing the ligand statistics for all models including cross-correlation, Qscore, and Bfactor.

> *(13) Style and Formatting Issues: format consistently throughout.*
>
> *(a) Kinetic Parameters: Please follow the IUPAC and IUBMB-recommended formatting:*
>
> *kcat should be italic with subscript.*
>
> *KM should be italic K with upright M.*
>
> *Use lowercase s^{-1}, not uppercase S^{-1}.*
>
> *Refer to:*
>
> *IUBMB enzyme nomenclature guidelines https://iubmb.org/wp-content/uploads/2021/01/Current_IUBMB_recommendations_on_enzyme_nomenclature.pdf*
>
> *IUPAC Green Book https://publications.iupac.org/books/gbook/green_book_2ed.pdf*

We have corrected the abbreviations according to the reviewers recommendations.

> *(b) Inconsistent Terminology and Typography:*
>
> *cryo-EM vs. cryoEM are used inconsistently - standardize throughout.*
>
> *FSC 0.143 appears with and without subscript formatting-please unify.*
>
> *Line 123: "X-ray" should be capitalized.*
>
> *Line 266: CryoEM should cryoEM, lowercase "c"*
>
> *Line 571: "100 µg ml^{-1}"-use superscript minus; ensure consistency with "mg ml^{-1}".*
>
> *Lines 605, 606, 626, 628: $MgCl_2$-ensure the $_2$ is subscripted throughout.*

> *Temperature units (lines 607, 630, 640): Write as "4 {degree sign}C" instead of "4C".*
>
> *Microliters (lines 660, 681, 697): Replace "uL" with "µL".*
>
> *Line 797: Use superscripts: K^+, Cl^-.*
>
> *Line 862: CO_2 should appear with subscript.*

We have made all terminology and typography consistent throughout based on these suggestions.

> ***Reviewer #2 (Recommendations for the authors):***
>
> *To strengthen the manuscript and address the methodological and interpretational gaps identified, we recommend the following revisions and additions:*
>
> *(1) Data processing and cryo-EM map quality*
>
> *(a) B-factor sharpening: Reprocess all cryo-EM maps using standardized B-factor sharpening workflows (e.g., the autoSharpen tool in cryoSPARC or similar methods) to enhance side-chain and ligand density visibility.*

We have updated main and supplementary figures to include sharpened maps. All maps were sharpened using the Autosharpen feature of Phenix, specifically, by half-maps. We have included in the methods section the following to reflect this change:

“Final cryo-EM maps were sharpened in Phenix using the Autosharpen feature by half-maps.”

> *(b) Document the specific parameters used (e.g., B-factor values, solvent content estimates) in the Methods section to improve transparency.*

See above regarding the additions made to the methods section.

> *(c) Map replacement and reanalysis: Replace all figures and supplementary panels displaying raw (unsharpened) maps (e.g., Figures 1D, 2D, 3A/B, 4A, 5B, and Supplementary Figs. 2D, S7B, S10) with the newly sharpened versions. Reanalyze density features (e.g., glutamine binding sites, ATP triphosphate groups) using these revised maps and update results to reflect any changes in interpretation.*

As requested, we have updated figures with sharpened maps and found our original analyses to hold. In particular, we have included multiple metrics of ligand model scoring in Supplementary Figure 7B including Q-score and CC. Additionally, we have included all ligand model statistics in Supplementary Table 2.

> *(2) Structural modeling and validation*
>
> *(a) Ligand fitting justification: Provide high-resolution ({less than or equal to}3 Å) density slices or side-chain density close-ups (e.g., for phenylalanine rings or glutamine-binding regions) to validate claims of atomic-level detail. For non-symmetric ligands (e.g., glutamine) fitted into symmetry-refined maps, explicitly describe how symmetry constraints were adjusted or applied during fitting (e.g., local symmetry refinement, manual adjustment of ligand orientation) and include validation metrics (e.g., cross-correlation scores, density fit plots) to support the placement.*

We have supplied 5 new supplementary figures to demonstrate the resolution of our sharpened cryo-EM maps (most notably Supplementary Figures 3, 4, 8, 12, 22 and panels in others) . Of particular note is the sharpened map features of R298A decamer under turnover conditions which demonstrates multiple instances of a ring density for aromatic residues.

See discussion above regarding the placement of glutamine in the interface density and updated handling of symmetry during refinement.

> *(b) Ligand density supplements: Include supplementary figures showing representative ligand-density fits (e.g., ATP, glutamine) with clear side-chain or functional group annotations, as is standard in structural biology publications.*

In our revision we have included the following updated figures and figure panels demonstrating ligand density into sharpened maps:

Turnover Filament Glutamine Ligand: Figure 2D-E (updated representation) and Supplementary Figure 7 (new and updated representations).

Turnover Filament ATP and Mg(II): Supplementary Figure 10 (updated representation)

Turnover Decamer ADP and Mg(II): Supplementary Figure 5 (new figure panel)

Turnover R298A ADP and Mg(II): Supplementary Figure 14 (new figure panel)

> *(3) Biochemical assay rigor*
>
> *(a) Control experiments: Perform and report the following controls to strengthen enzyme activity claims:*
>
> *- A blank control (reaction mixture without GS, ammonia, or glutamate) to quantify background ATP hydrolysis.*
>
> *- Substrate omission controls (reactions lacking ammonia or glutamate) to confirm that ATP hydrolysis depends on both substrates and GS catalysis.*
>
> *- A TCEP effect control (compare ATP hydrolysis rates with and without TCEP) to rule out reducing agent interference with the PK/LDH coupled assay.*

We have provided blank, substrate omission, and TCEP controls in Supplementary Figure 1. These results demonstrate negligible ATP hydrolysis without complete substrate inclusion and do not indicate any impact from TCEP inclusion.

> *(b) Direct activity validation: Consider supplementing the coupled assay with a more direct measure of GS activity (e.g., quantifying inorganic phosphate release via malachite green assay) to cross-validate results.*

On the merits of the PK/LDH coupled assay being used for >55 years to measure steady-state activity of glutamine synthetases and that it is a robust assay as supported by the additional control experiments presented above in Supplementary Figure 1 we have elected not to pursue tedious cross-validation with a non-continuous assay and believe our interpretation of the enzyme kinetic results hold.

> *(4) Writing and presentation clarity*
>
> *(a) Methods detail: Expand the Methods section to explicitly describe:*
>
> *- Cryo-EM data processing steps, including B-factor sharpening parameters, map reconstruction workflows, and any post-processing (e.g., filtering, masking).*
>
> *- Criteria used to validate ligand fitting (e.g., density threshold values, manual vs. automated docking).*

See above the revisions made in response to critique from review #1 which we will briefly summarize here:

We have included in the methods section the following to reflect this change:

“Final cryo-EM maps were sharpened in Phenix using the Autosharpen feature by half-maps.”

Focused masks are represented in Figure 2E, Supplementary Figure 18, and Supplementary Figure 19. The details around focused mask utilization are included in the revised figure captions and the following was included in the Methods.

“Focused masks were generated in ChimeraX (v.1.7 and above). Focused refinement and 3D classification (3 Å filter resolution, PCA initialization) were performed in cryoSPARC. Strategy of class picking and refinement are noted in Supplementary Figures 18 and 19.”

Map reconstruction workflows are present in the relevant Supplementary Figures. No post-processing steps beyond map sharpening in Phenix were carried out. In general, human GS represents a straightforward protein to reconstruction via cryo-EM.

Ligand identification criteria was described throughout the results section. Supplementary Figure 7 was revised to show sharpened density for either globally refined or locally refined maps fit with all three products of the glutamine synthetase reaction (ADP, Pi, and glutamine) individually showing the best CC and Qscore for glutamine. Beyond Supplementary Figure 7 we also combined both biochemical experiments and cryoEM to make this ligand assignment supported by:

(1) Time-resolved cryo-EM experiments that show increasing filament particles over reaction time (Figure 2B and Supplementary Figures 9 and 10)

(2) Glutamine+ATP cryo-EM screening (Figure 2C) showing long filaments

(3) Supplementary Table 2 showing reasonable ligand statistics for glutamine

To clarify this in the Methods sections we include the following statement:

“Ligands were placed with ISOLDE (v1.7) and those with >0.5 Qscore and supporting biochemical and/or literature precedent were built.”

> *(b) Results framing: In the Results, clearly distinguish between observations supported by sharpened maps and preliminary/unvalidated features. Avoid over interpreting density in unprocessed maps (e.g., referring to "glutamine binding" in Figure 2D without noting current density limitations).*

We have updated our discussion of Figure 2D (and now also Figure 2E) to include discussion of only sharpened maps and noted current density limitations to the interpretation.

> *(5) Data and material availability*
>
> *(a) Ensure all supporting data are publicly accessible:*
>
> *- Upload raw cryo-EM movies, particle stacks, and processed maps to the Electron Microscopy Data Bank (EMDB) with appropriate accession codes.*
>
> *- Deposit final atomic models in the Protein Data Bank (PDB) and reference these accession codes in the manuscript.*

We deposited maps and models with accession codes in advance of review. The PDB and EMDB codes are available in Supplementary Table 1.

Furthermore, for the focused maps and focused classifications that were generated during the review, and for the benefit of not cluttering the PDB/EMDB, we have included these more specific analyses in Zenodo: 10.5281/zenodo.20298855.

> *- Provide detailed protocols for biochemical assays (e.g., TCEP handling, enzyme purification) in the Methods or as supplementary information to enable reproducibility.*

See updates above to reviewer #1

> *(b) By implementing these revisions, the manuscript will better align with eLife's standards for methodological rigor, transparency, and reproducibility, allowing readers to confidently evaluate the study's contributions to structural and functional biology.*

We agree!

> ***Reviewer #3 (Recommendations for the authors):***
>
> *(1) In line 252, it would be helpful to show negative-stain EM images for each SEC peak, further probing whether any peaks correspond to partially aggregated, as this could affect the measured Kcat and Km.*

We aren't in a position to do this experiment. We routinely check for aggregation by noting Absorbance at 340nm for non-specific scattering indicative of aggregation and observed no evidence of aggregation in our fractions.

> *(2) In Supplementary Figure 6, many of the classes in the "Selected Filament Classes" inset appear to be averages of closely spaced particles, which may bias the calculation and should be excluded. In the "Selected Decamer Classes", I would suggest removing the top-view particle classes, as these particles not only have significantly different ice penetration rates, but are also more difficult to distinguish in 2D classification.*

We agree and have provided an additional, more strenuous cutoff, analysis of the tr-cryo-EM data wherein only classes that show clearly aligned decamers are included and all top views are omitted (Additional Supplementary Figure 6). We are happy to say that even with the more strenuous cutoffs that our main conclusions that filaments increase with forward reaction time holds.

> *(3) In line 445, "Figure 5A" should be corrected to "Figure 5B".*

We thank the reviewer for pointing this out and have made the correction.

https://doi.org/10.7554/eLife.108336.2.sa0